UNIVERSITÀ DEGLI STUDI DI CATANIA

IN CONVENZIONE

UNIVERSITÀ DEGLI STUDI DI PALERMO

DOTTORATO DI RICERCA IN

SCIENZA DEI MATERIALI E NANOTECNOLOGIE - XXIX CICLO

Giuffrida Antonino Emanuele

SURFACE ENGINEERED NANOSTRUCTURED OXIDES AS MULTIFUNCTIONAL MATERIALS FOR ENVIRONMENTAL AND BIOMEDICAL APPLICATIONS

TUTOR: Chiar.mo Prof. G. G. Condorelli

COORDINATORE: Chiar.ma Prof. M. G. Grimaldi

TESI PER IL CONSEGUIMENTO DEL TITOLO DI DOTTORE DI RICERCA

"I chimici sono una strana classe di mortali, spinti da un quasi folle impulso nel ricercare piacere tra fumo e vapore, fuliggine e fiamme, veleni e povertà; eppure tra tutti questi mali mi sembra di vivere così dolcemente che potrei morire se dovessi scambiare la mia vita con quella del principe di Persia"

"The chemists are a strange class of mortals, impelled by an almost insane impulse to seek their pleasures amid smoke and vapour, soot and flame, poisons and poverty; yet among all these evils I seem to live so sweetly that may I die if I were to change places with the Persian king"

(Johann Joachim Becher)

Indice

Aim of the work

The main topic of this thesis is the surface modification of nanostructures of metals oxides with molecular monolayers in order to obtain multifunctional materials suited for environmental and biomedical applications. In particular, the oxides under investigation have been nano columns of ZnO and superparamagnetic Fe_3O_4 nanoparticles, for which the intrinsic properties of the nanostructured oxides have been combined with specific functional molecules in order to obtain new functional materials suited for environmental or biomedical applications.

In all the reported cases, the synthetic strategy used for the preparation of active surfaces is based on a two steps approach based of a first pre-functionalization of the oxide surface with a phosphonic linker followed by the anchoring of one or more functional molecules. A key point in the design of the molecular monolayers is the presence of cavitands, versatile receptors having a rigid cavity and bearing four branches. The combination of the inorganic nanostructures with the cavitand receptors in an hybrid material and the evaluation of its functional properties is the central issue of this thesis.

Chapter 1: State of art

1.1 Introduction

1.1.1 Nanotechnology and nanomaterials

In 1959 Richard Feynman, Nobel prise winner, first proposed the idea of nanotechnology, suggesting the development of molecular machines, and since that the scientific community has investigated the role that nanotechnology can play in every aspect of our society. This field of investigation is so interesting that in 2016 the Nobel prise for Chemistry was awarded at Jean-Pierre Sauvage, J. Fraser Stoddart and Bernard L. Feringa for the design and synthesis of molecular machines. This term (nanotechnology) refers to the research and the technology development at atomic, molecular, and macromolecular scale, which leads to the controlled manipulation and study of structures and devices with length scales in the range of 1-100 nanometers. One nanometer (nm) is one billionth of a metre; tens of thousands of times smaller than the width of a human hair (Fig. 1.1).

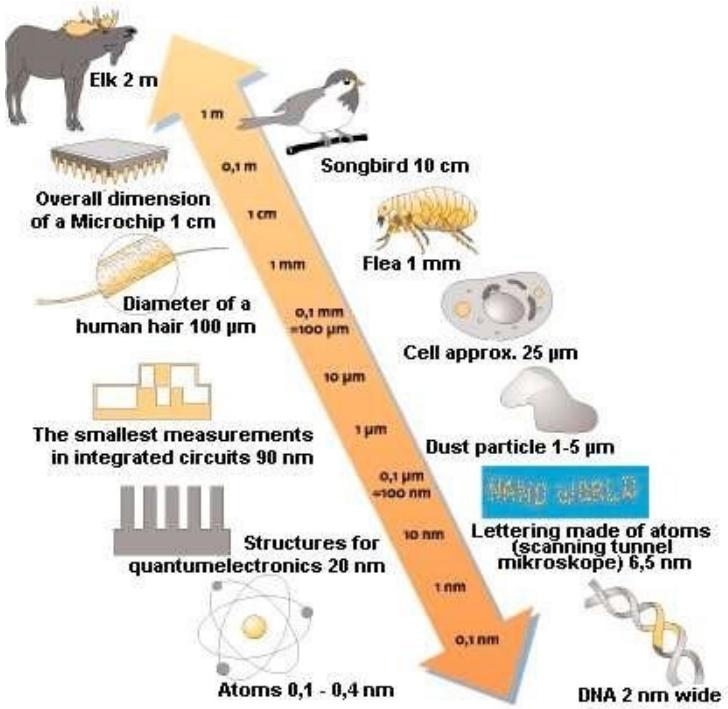

Figure 1. 1 Objects of approximate size from 1 m to 10-10 m.

In the last fifteen years, the research in the field of nanotechnology has grown exponentially with over twenty-nine thousand papers according to Web of Science. [1]

The allure of nanotechnology comes from the possibility to control the properties of the material assembling such building-blocks at the nanoscale. Moreover, the tunability of such materials were stated in Norio Taniguchi's paper in 1974

where the term ‘‘nanotechnology’’ was first used in a scientific publication. Recently, nanomaterials, which are materials with basic structural units, grains, particles, fibres or other constituent components smaller than 100 nm in at least one dimension, have evoked a great amount of attention for their theoretical issues and applicative potentialities. [2] In fact, nanostructured materials with tunable morphology are intresting because of their unique architectures, tailored physicochemical properties, central roles in fabricating nanoelectronics, and potential applications in bionanotechnology. In recent years, an extended array of novel nanostructures have been manufactured and studied in the interdisciplinary fields of nanoscience, material science, biological science, etc. Thus far, lots of investigations with respect to inorganic nanomaterials have been reported and well documented, as summarized by various review articles.[3] Compared with inorganic ones, the organic counterparts have, in particular, fascinated scientists because of their multifunctionality, considerable variety and flexibility in molecular design, and solution processability. These advantages make the organic nanostructures promising candidates for electronics, including organic field-effect

transistors, organic light emitting displays, nanosensors, etc. Thus, the exploration of the controlled synthesis of organic nanostructures is a significant issue. [4]

1.1.2 Self Assembled Monolayer

Self-assembled monolayers (SAMs) are organic assemblies formed by the adsorption of molecular constituents from solution or gas phase onto the surface of solids or in regular arrays on the surface of liquids (in the case of mercury and probably other liquid metals and alloys); the adsorbates organize spontaneously (sometimes epitaxially) into crystalline (or semi-crystalline) structures.[5]

The term “self-assembling monolayer” was adopted for the first time in 1978 on Topics in Surface Chemistry in a chapter written by Dietmar Mobius that describes this technique among others used to assembling and manipulating monolayers.[6] The self-assembly of adsorbates on an appropriate surface is known since 1946, when Zisman and co-workers reported the formation of monomolecular films of long-chain hydrocarbons carrying polar groups on a variety of polar surfaces.[7,8] Although these films are extremely thin (typically ca. 2 nm), they are able to change the surface properties completely.

However, the versatility of these adsorbed monolayers was not realized until 1978, when Polymeropoulos and Sagiv proposed their use for measuring electrical conduction between two metal surfaces.[9] In 1980, Sagiv published the first article demonstrating the formation of well-defined organosilane monolayers on SiO_2 by direct adsorption (that is, self-assembly) from solution.[10,11]

Nowadays it is well known that self-assembled monolayers (SAMs) provide a convenient, flexible, and simple way to customize interfacial properties of metals, metal oxides, and semiconductors.

The method of self-assembled monolayers (SAMs) has risen exponentially in synthetic sophistication and depth of characterisation over the last two decades, in fact the Figure 1.2 represents the increasing number of articles/reports published per year in the fields of SAMs in the last two decades. The success of SAMs is due likely to their ability to create controlled surface chemistry with high molecular organization and defined stoichiometry over relatively large areas.

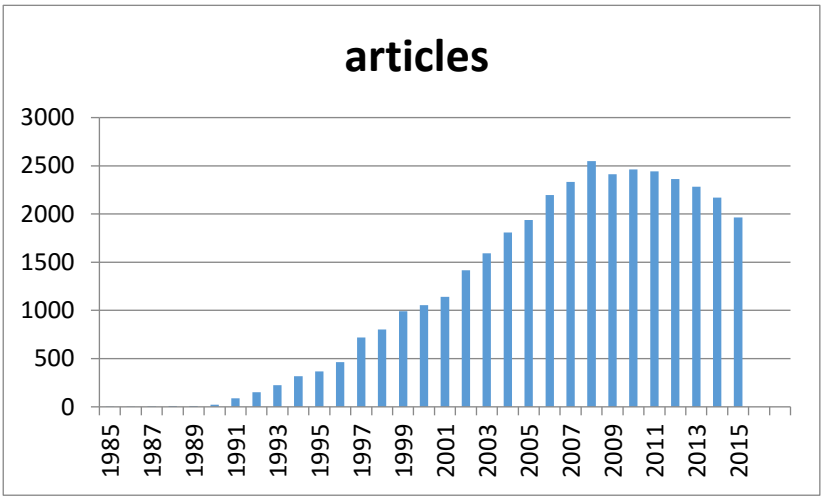

Figure 1. 2: Numbers of published article addressing self-assembled monolayers.

SAMs have simplified the study of molecular and cellular interactions with specific functional groups, surface energetic, surface charge, or other interface properties. SAMs can be used to include specific functionalities or ligands to study biological interactions such as cell signalling, cell adhesion [12] and protein interactions.[13,14] SAMs have also been used for constructing molecular switches,[15] biosensors[16] and microarrays. SAMs offer a unique combination of physical properties that allow fundamental studies of interfacial chemistry, solvent-molecule interactions and self-organization.

1.1.3 Basics of SAMs

A scheme of an organic SAM array is shown in Figure 1.3. Usually, SAMs are formed spontaneously by dipping such substrates into an active solution, e.g. surfactant molecules $R(CH_2)_nSiX_3$ (X = Cl, OCH3 or OC2H5) dissolved in alkane/carbon tetrachloride solvent; however, the SAMs can be deposited by other techniques such as vapour deposition.

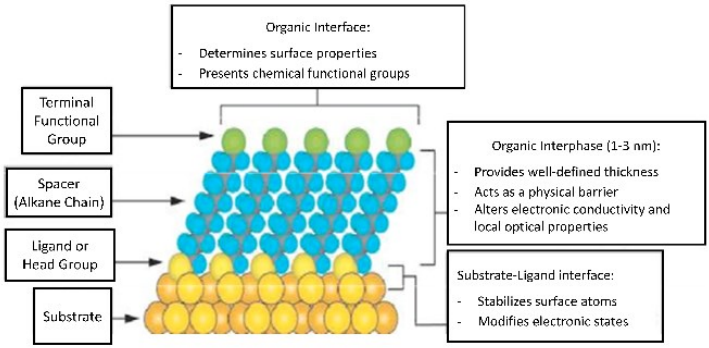

Figure 1. 3: A schematic diagram showing different parts of a self-assembled monolayer on a metal surface.

The self-assembling monolayer can be divided into three parts:

1) Head group. It forms the chemical bond with surface atoms of the substrate causing the pinning of surfactant molecule to the substrate.

2) Alkyl chain. The inter-chain van der Waals interactions could assist the formation of an ordered molecular structure. Of course, the possibility of obtaining ordered structures depends on the pinning density of the head groups.
3) Surface group. This is the terminal group which is replaced with or bonded to different functional groups to obtain specific applicative devices.

1.1.4 Characterization of SAMs

The quality of deposited SAMs is assessed determining their thickness, molecular orientation and/or ordering, uniformity of coverage, chemical composition, thermal and chemical stability.

Various techniques are available for the characterization of monolayers[17]. The chemical composition of monolayers can be determined by Auger electron spectroscopy (AES), X-ray photoelectron spectroscopy (XPS) and secondary ion mass spectroscopy (SIMS). In particular, XPS is a reliable technique to settle the chemical composition of organic ultrathin layers on such substrates. In the XPS instrument, the photoelectrons that are able to escape from substrate's surface are analysed with respect to their kinetic energy and the core level binding

energies of those electrons can be determined. Thanks to this technique it can be afford information about the chemical composition (elemental distribution and chemical state of the elements) of the examined sample.

1.2 Chemical Sensors

Since 80's the interest on chemical sensors have been growing because of the widespread use of those systems in several areas of daily routine such us environmental monitoring, public security and food safety. Nowadays, the rising interest for this kind of technology is fostered by the increasing efforts in biochemical, bio-reactions and nanomedicine.

In fact, billions of dollars are spent in equipment related to medical diagnosis but usually those are cumbersome and time-consuming. Therefore, there is a pressing need towards cheaper and easier chemo/biosensors for the detection of various analytes in solution and atmosphere. Only few chemo/biosensors for simple analytes have been able to meet commercial requirements with detection sensitivity, selectivity, accuracy and reliability approaching that of experimental equipment. However, the recent developments of novel chemosensory materials and fabrication technologies

may provide many potential opportunities for the development of a new generation of chemo/biosensors. Thus, the explorations on chemo/biosensors based on novel sensing concept have attracted growing interest in recent years.[18]

A chemical sensor is a device that transforms chemical information, ranging from the concentration of a specific sample component to total composition analysis, into an analytically useful signal.

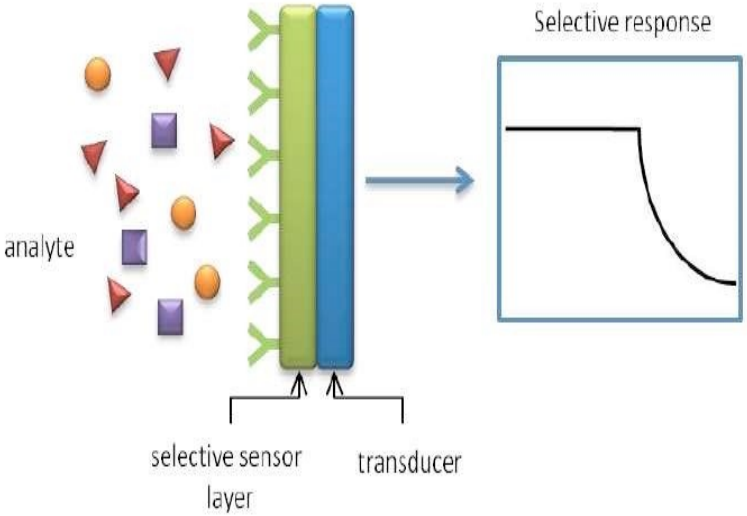

Figure 1. 4: Working principle of supramolecular sensors.

The chemical information, mentioned above, may originate from a chemical reaction of the analyte or from a physical

property of the system.[19] The sensing material interacts with a chemical species present in the environment, called analyte, by changing some of its physicochemical properties, while the transducer transforms these variations into a readable signal. The structure of a generic chemical sensor is shows in Figure 1.4.

Chemical sensors contain two basic functional units: a receptor part and a transducer part.

In the ***receptor*** part of a sensor the chemical information is transformed into a form of energy which may be measured by the transducer.

The ***transducer*** part is a device capable of transforming the energy carrying the chemical information about the sample into a useful analytical signal. The transducer as such does not show selectivity.

The receptor part of chemical sensors may be based upon various principles:

1) Physical, where no chemical reaction takes place. Typical examples are those based upon measurement of

absorbance, refractive index, conductivity, temperature or mass change.

2) Chemical, in which a chemical reaction with participation of the analyte gives rise to the analytical signal.
3) Biochemical, in which a biochemical process is the source of the analytical signal. Typical examples are microbial potentiometric sensors or immunosensors. They may be regarded as a subgroup of the chemical ones. Such sensors are called ***biosensors.***

Chemical sensors may be also classified according to the operating principle of the transducer[20] in:

Optical devices, wich transform changes of optical phenomena, which are the result of an interaction of the analyte with the receptor part. This group may be further subdivided according to the type of optical properties which have been applied in chemical sensors.

Electrochemical devices, wich transform the effect of the electrochemical interaction analyte-electrode into a useful signal. Such effects may be stimulated electrically or may result in a spontaneous interaction at the zero-current condition.

Electrical devices, based on measurements, where no electrochemical processes take place, but the signal arises from the change of electrical properties caused by the interaction of the analyte.

Mass sensitive devices, wich transform the mass change at a specially modified surface into a change of a property of the support material. The mass change is caused by accumulation of the analyte.

Magnetic devices based on the change of paramagnetic properties of a gas being analysed. These are represented by certain types of oxygen monitors.

Thermometric devices based on the measurement of the heat effects of a specific chemical reaction or adsorption which involve the analyte. In this group the heat effects may be measured in various ways, for example in the so called catalytic sensors the heat of a combustion reaction or an enzymatic reaction is measured by use of a thermistor.

Sensors are typically characterized by three properties: *sensitivity*, *selectivity* and *reversibility*.

Sensitivity can be generally defined as the slope of the analytical calibration curve, that is correlated with the magnitude of the change in the sensor signal upon a certain change in the analyte concentration.[21] "Cross sensitivity" hence refers to the contributions of other than the desired compound to the overall sensor response.

Selectivity is instead the ability of a sensor to respond primarily to only one chemical species in the presence of different species (usually denoted interferents). The quest for better selectivity remains the main target of the chemical sensing research,[22] it can be achieved by using biosensors (e.g. biologically derived selectivity by appropriate enzymes, structure-binding relationship in antibodyantigen complexes,) or by synthesizing materials containing specific binding sites.

Reversibility describes the sensor's ability to return to its initial state after it has been exposed to analytes and more in general chemical species. For the reversibility to take place it requires the formation of weak interactions, since the formation of covalent or ionic bonds would result in an irreversible saturation of the layer.[23]

The conventional design of chemical sensors uses a “lock-and-key” approach (a steric fit concept enunciated for the first time by Emil Fischer in 1894),[24] wherein a specific receptor is synthesized to bind the analyte strongly and selectively.

This concept has been widely exploited by supramolecular chemists for the design and synthesis of molecular receptors which are useful to understand and mimic nature specific interactions. As for biological systems, the concepts of shape recognition and the complementarity of binding site are central issue for effective molecular recognition in artificial host-guest systems. The efforts that have been done in seeking the best design in the field of synthetic receptors[25] allow sensor selectivity modulation towards different classes of compounds by mastering the weak interactions that occur between the sensing material and the analytes. The selective binding of a neutral substrate by a molecular receptor to form a complex (molecular recognition) is based on shape complementarity and also on the presence of specific interactions such as hydrogen bonding,[26] stacking,[27] and CH-π interactions.[28] Molecular recognition is a concept really attractive and potentially powerful approach to engineering structures and devices at the molecular scale.[29]

Organic monolayers hosted on inorganic surfaces[30-35] represent the best approach to use the full potential of molecular recognition on surfaces.[36,37] Compared to both thin films and bulk materials containing molecular receptors, such hybrid organic-inorganic materials have the advantage of reducing or even eliminating non-specific interactions which often mask the recognition events.[38] There is a wide choice of host molecules; such examples of very promising host system are: crown ethers, cavitands, cyclodextrins and calixarenes.

1.3 Environmental Remediation

Avoiding or limiting the inlet of contaminants or wastes in the environment should represent a fundamental aspect of life cycle in any industry, but, unfortunately, this is not always true. For this reason, today more than ever, there is an increasing quest for environmental remediation programmes by all media such as soil, groundwater, sediment, or surface water.[39] Fortunately, taking care of the environment today is a sustainable challenge and nanomaterials represent a technological advanced and suitable way to remove such

pollutants. The interest for the application of such nanosystems in environmental remediation is raising so much that they coined a word to described this field of application, nanoremediation. During a nanoremediation process, a nanoparticle agent must be brought into contact with the target contaminant under conditions that allow a detoxifying or immobilizing reaction. This process typically involves a pump-and-treat process or in situ application.

Compared to conventional macroscale materials, nanomaterials exhibit significant improvements in surface area as a function of mass. Additionally, their colloidal size allows subsurface deployment via injection with the rapid treatment of aqueous contaminants at almost any location and depth in terrestrial groundwater systems.

Conceptually, the key properties required for the use of any engineered nanoparticle for in situ remediation of polluted groundwater are:

1) high reactivity for contaminant removal;

2) sufficient mobility within porous media;

3) sufficient reactive longevity;

4) low toxicity.

These properties are operational drivers and at the same time the material must be manufactured and deployed at a cost that is competitive with other existing technologies. Not many engineered nanoparticles fulfil the above mentioned requirements.

1.4 Enhanced Drug Delivery Systems

Targeted drug delivery is a very interesting field that in the last decade has been developing faster than ever. This method allows to deliver medication to a patient in a faster and more efficient manner increasing the concentration of the drug in some specific parts of the body.

Considering the fact that about 1.5 billion people worldwide suffer from brain diseases and moreover the growing demand for cancer therapies for a sick population, there is a clear need for a suitable strategy to deliver non-permeating therapeutic agents.[40,41]

Although effective drugs are available for such disorders, their application is limited because of their low distribution inside

the cells or inability to cross the Cell Barrier. For example, most of the drugs systematically administered for chemotherapy do not gain access to the brain in the required concentration for tumours. It has been proposed that small molecules (molecular weight < 400 Da) with high lipophilicity that are not substrates for active efflux transporters, cross the BBB. However, more than 98% of small molecules do not meet these requirements to enter the brain. In addition, 100% of large molecules are unable to gain entry to this organ.

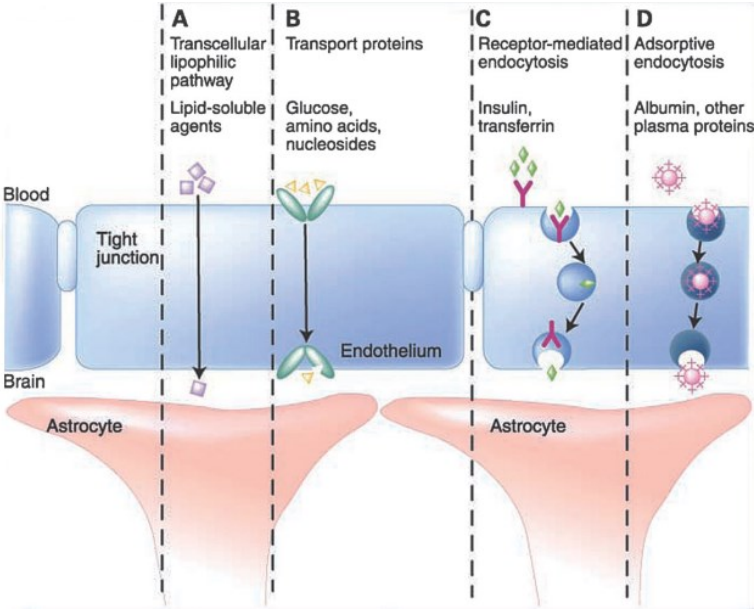

Figure 1. 5: Schematic representation of the mechanisms available to transport endogenous molecules across the BBB

In fact, compounds cross the BBB by means of active or passive mechanisms (Figure 1.5).

In passive targeting, the drug's success is directly related to circulation time. This is achieved by cloaking the nanoparticle with some sort of coating. Several substances can achieve this, e.g. polyethylene glycol (PEG). By adding PEG, the surface of the nanoparticle turn to be hydrophilic, thanks to the oxygen atoms of PEG. The efficient solvation of the

nanoparticle makes the substance antiphagocytic thus allowing to stay in circulation for a longer period of time.[42] To work in conjunction with this mechanism of passive targeting, nanoparticles that are between 10 and 100 nanometers in size have been found to circulate systemically for longer periods of time.[43]

By contrast, the active targeting of drug-loaded nanoparticles enhances the effects of passive targeting to make the nanoparticle more specific to a target site. There are several ways in which this mechanism can be accomplished. Knowing the nature of the receptor on the cell is a way to target a drug, so a specific ligand can be utilized; this leads to bind specifically to the cell that has the complimentary receptor. Active targeting can also be achieved by utilizing magnetoliposomes, which usually serves as a contrast agent in magnetic resonance imaging (MRI).[44] Thus, by grafting these liposomes with a desired drug to deliver to a region of the body, magnetic positioning could aid with this process.

Furthermore, a nanoparticle could possess the capability to be activated by a trigger that is specific to the target site, utilizing, as example, materials that are pH or redox potential responsive.[43]

In order to achieve the goal of efficiently transport drugs inside the cell barrier, the approach largely used in nanomedicine plans to employ nanoparticle-mediated drug delivery strategy in order to avoid the downfalls of conventional drug delivery. The nanoparticles would be loaded with drugs and targeted to specific parts of the body where there is diseased tissue, thereby avoiding interaction with healthy tissue. Ideally the goal of a targeted drug delivery system should be to prolong, localize, target and have a protected drug interaction with the diseased tissue. The advantages are the reduction in the frequency of the dosages taken by the patients and the reduction of drug's side-effects. The disadvantage of the system is the reduced ability to adjust the dosages.

1.5 Cavitands

Cavitands are a class of complex organic compounds that have been synthesized for the first time by Cram and co-workers whom define them as "synthetic organic compounds with enforced concave cavities large enough to complex complementary organic molecules or ions"[45], whose

complexation properties have been extensively studied at solid state[46], in solution[47] and in the gas phase.

The concave surface allows the docking of different functional groups on the substrate binding sites theoretically inaccessible because located inside the cavity.[48]

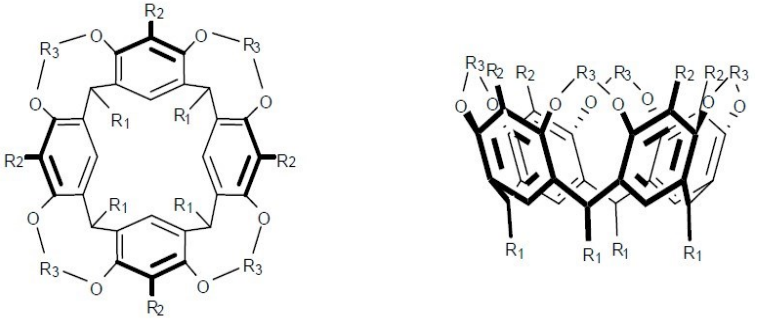

Figure 1. 6: Structure of a cavitand top (left) and side(right) views

Cavitands are generally synthesized by covalent linkage of neighbouring phenolic hydroxyl groups in the corresponding octols. They are particularly attractive because the rim of the bowls can be varied with different R_2 substituent and bridging groups R_3 for deepening the bowl cavity and for introducing potentially cooperating functional groups to act as molecular receptors.[49] Moreover the R_1 substituent can be used for changing the solubility or the morphology in the solid state. A already said, cavitands are designed to bind target molecules

to form host-guest complexes with a variety of guest molecules and ions through their rigid, concave π-basic cavity, which enables electrostatic interactions such as cation-π and CH-π. In addition, appropriate substitution at the upper-rim allows them to employ hydrogen bonding in the formation of complexes.

The most common bridging groups are alkylenedioxy, dialkylsilicon, heterophenylene and phosphoryl.

In this thesis we focalized the attention on two kinds of cavitands: phosphourus-bridged, quinoxaline-bridged.

1.5.1 Quinoxaline-Salen-bridged cavitands

The cavity of resorcinarenes can be largely extended by bridging phenolic hydroxyl groups with aromatic spacers.[5051] Tetraquinoxaline cavitands result from nucleophilic aromatic substitution with 2,3-dichloroquinoxaline on the phenolic oxydryl moieties of a resorcin[4]arene.

A peculiarity of these systems is the reversible switching between a closed “vase” conformation with a deep cavity for guest complexation, and an open “kite” conformation with a

flat extended surface.[52] Indeed the quinoxaline spacers can occupy either axial (a) or equatorial (e) positions (Figure 1.7). In the "vase" (aaaa) conformer, the spacers touch each other via their hydrogens while forming a box like cavity with C4V symmetry which is approximately 7 Å wide and 8 Å deep.[53] The cavity is open at the top and closed at the bottom by the cavitand itself. In the "kite" (eeee) conformer, the spacers are more or less in the same plane (C_{2v} symmetry). Conformational switching can be reversibly induced by temperature or pH changes (the "kite" conformation is preferred at low temperatures and low pH values), or by metal-ion addition.

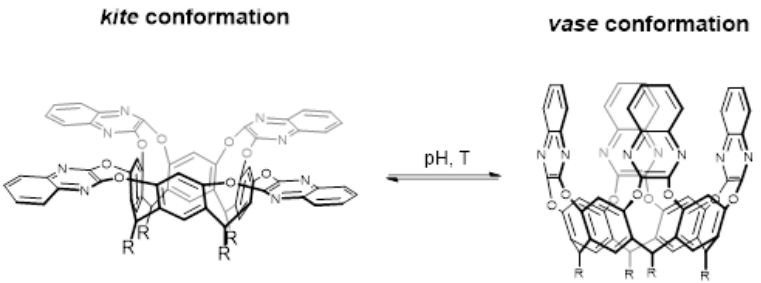

Figure 1. 7: Structure of quinoxaline cavitand eeee conformer (left) and aaaa conformer (right)

In contrast, in mixed-bridged cavitands with one of the four quinoxaline wings displaced by a different bridge, the thermal

vase-to-kite interconversion is switched off by substantially decreasing of the solvation of the kite form. Mixed-bridged cavitands can therefore adopt only the kite conformation by protonation of the quinoxaline nitrogen atoms with an acid such as TFA, as a result of the developing Coulombic repulsion in the vase geometry.

New mixed-bridged triquinoxaline (3QxCav) are proposed as receptor for the realization of materials to be used as trapping devices for nitroaromatic compounds.

The receptor discussed in this thesis consists of a QxCav compound functionalized with four alkyne functionalities.

1.5.2 Phosphorous bridged Cavitands

The first attempt to synthesize phosphorous-bridged cavitands was carried out in Cram's group in the '80s by reacting a methyl-footed resorcin[4]arene with dichlorophenylphosphonate, obtaining a mixture of diastereomers difficult to isolate.[54]

In fact, the presence of four P^{v} stereogenic centers paves the way to six possible diastereomeric cavitands. The inward (i)

and outward (o) configurations are defined relative to the different orientation of the P=O moieties (Figure 1.8)

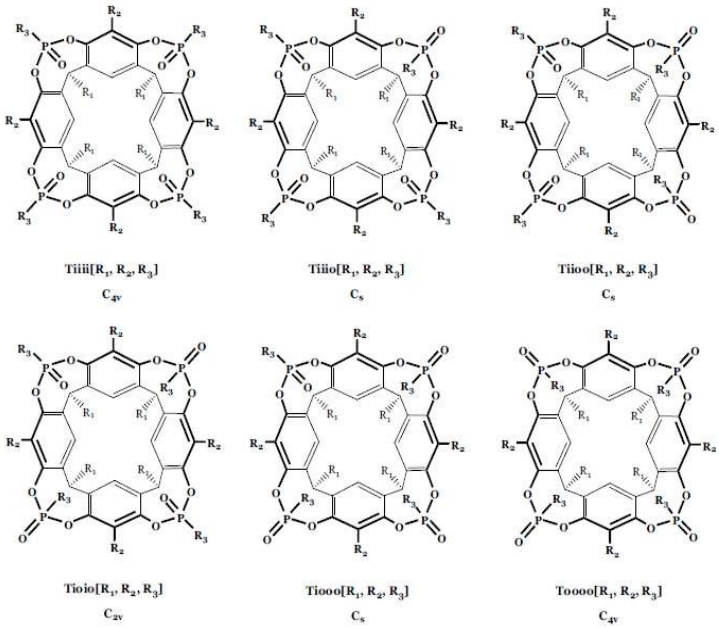

Figure 1. 8: Isomers of tetraphosphonate bridged cavitands.

The tetraphosphonate cavitands nomenclature, reported in Figure 1.8, summarizes the number and relative positions of P^v bridges, their stereochemistry, and the type of substituents at the lower rim, at the apical positions, and on the phosphorus bridges, respectively, in a single term.

In particular, the capital letter, defines number and nature of bridges, the lower case letters define the in-out stereochemistry, and R_1, R_2 and R_3 in brackets define the substituents at the lower rim, in the apical positions and on the phosphorous stereocenters respectively.

Tetraphosphonate cavitand presents remarkable recognition properties toward N-methylpyridinium ($K_{ass} \sim 10^7$, Figure 1.9 a) and N-methylammonium ($K_{ass} \sim 10^9$, Figure 1.9 b) which can be attributed to three synergistic interaction modes:

1) $N^+ \bullet\bullet\bullet O{=}P$ cation-dipole interactions;
2) CH_3- interactions of the acidic $^+N\text{-}CH_3$ group with the basic cavity;
3) two simultaneous hydrogen bonds between two adjacent P=O bridges and the two nitrogen protons,[55] in the case of protonated secondary amines;

The simultaneous hydrogen bonds are the reason for the higher affinity of the N-methylammonium toward the cavity.

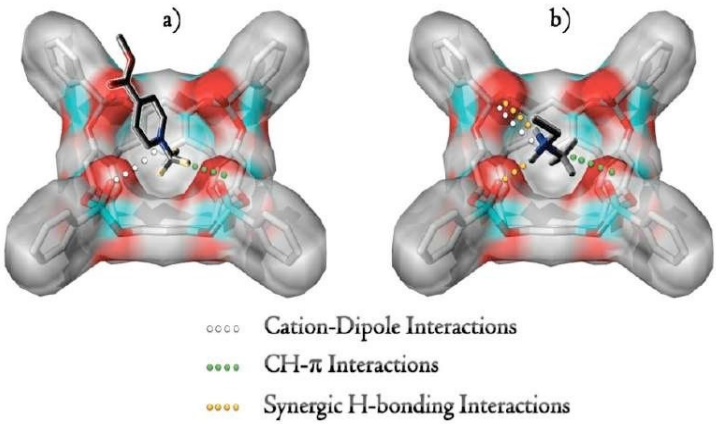

Figure 1. 9: Interactions involved in the molecular recognition process.

Another class of cavitand (TS_{iiii}), structurally identical to the 4PO receptor except for the presence of four P=S instead of four P=O has been synthesized via oxidation in situ of the tetraphosphonite cavitand with S_8.

This substitution strongly reduces the molecular recognition properties, because sulphur has lower electronic density with respect to the oxygen and consequently less affinity for H-bonding interactions.[56] In addition the cavity of TS_{iiii} is much smaller and less prone to guest inclusion because sulphur is larger (atomic radius=1 Å) than oxygen (atomic radius=0.6 Å). (Figure 1.10)

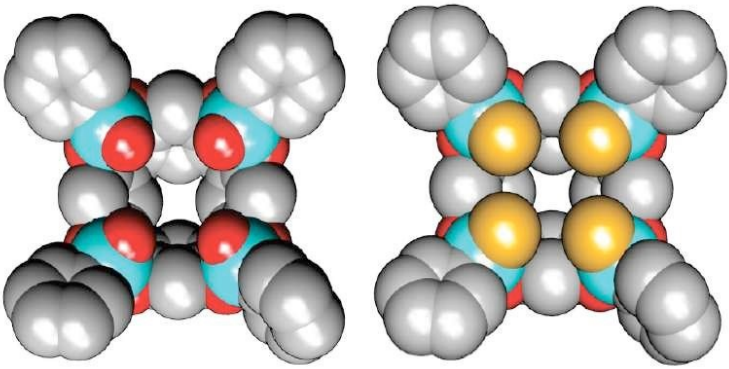

Figure 1. 10: Comparison between tetraphosphonate (left) and tetrathiophosphonate (right) cavitands (top view).

[1] J. Gao, B. Xu, *Nano Today*, **2009**, 4, 37-51.

[2] L. Zhang, T. J. Webster, *Nano Today*, **2009**, 4, 66-80.

[3] a) C. Bae, H. Yoo, S. Kim, K. Lee, J. Kim, M. M. Sung, H. Shin, *Chem. Mater.* 2008, 20, 756–767. b) G. R. Patzke, F. Krumeich, R. Nesper, *Angew. Chem., Int.Ed*. **2002**, 41, 2446–2461. c) S. J. Hurst, E. K. Payne, L. Qin, C. A. Mirkin, *Angew. Chem., Int. Ed.* **2006**, 45, 2672–2692. d) B. Tian, T. J. Kempa, C. M. Lieber, *Chem. Soc. Rev.* **2009**, 38, 16–24.

[4] Y. Qiu, P. Chen, M. Liu, *J. Am. Chem. Soc.*, **2010**, 132, 9644-9652.

[5] J. C. Love, L. A. Estroff, J. K. Kriebel, R. G. Nuzzo, G. M. Whitesides, *Chem. Rev.* **2005**, 105, 1103-1169.

[6] Möbius, D. in Topics in Surface Chemistry (eds. Paul S., B. & Kay, E.) 75–101 (*Springer US*, **1978**). doi:10.1007/978-1-4613-4003-4_4

[7] W. C. Bigelow, D. L. Pickett,W. A. Zisman, *J. Colloid Sci.* **1946**, 1, 513.

[8] W. C. Bigelow, E. Glass, W. A. Zisman, *J. Colloid Sci.* **1947**, 2, 563.

[9] E. E. Polymeropoulos, J. Sagiv, *J. Chem. Phys.* **1978**, 69, 1836.

[10] J. Sagiv*, J. Am. Chem. Soc.* **1980**, 102, 92.

[11] S. Onclin, B. J. Ravoo, D. N. Reinhoudt, *Angew. Chem. Int. Ed.* **2005**, 44, 6282-6304.

[12] C. Tidwell, S. Ertel, B. Ratner, B. Tarasevich, S. Atre, D. Allara, *Langmuir* **1997**, 13, 3404-3414.

[13] R. E. Holmlin, X. Chen, R. G. Chapman, S. Takayama, G. M. Whitesides, Langmuir, **2001**, 17, 2841-2850.

[14] E. Ostuni, R. G. Chapman, M. N. Liang, G. Meluleni, G. Pier, D. E. Ingber, G. M. Whitesides, *Langmuir*, **2001**, 17, 6336-6343.

[15] C. Engtrakul, L.R. Sita, *Nano Lett.*, **2001**, 1, 541-549.

[16] J. J. Gooding, F. Mearns, W. Yang, J. Liu, *Electroanal.,* **2003**, 15, 81-96.

[17] M. Kind, C. *Woll Progress in Surface Science*, **2009**, 84, 230–278.

[18] G. Guan, B. Liu, Z. Wang, Z. Zhang *Sensors* **2008**, 8, 8291-8320.

[19] A. Hulanichì, S. Geab, F. Ingman, *Pure&App. Chern.*, Vol. 63, No. 9, pp. 1247-1250, **1991**.

[20] R. W. Cattrall, Chemical Sensors, *Oxford Science Publications*, **1997**.

[21] A. D'Amico, C. Di Natale, *IEEE Sensors Journal* **2001**, 1, 183.

[22] J. Janata, M. Josowicz, *Anal. Chem.* **1998**, 70, 179.

[23] A. Hierlemann, A. J. Ricco, K. Bodenhöfer, W. Göpel, *Anal. Chem.* **1999**, 71, 3022.

[24] E. Fischer, *Ber. Dtsch. Chem. Ges*. **1894**, 27, 2985.

[25] J.-M. Lehn, *Supramolecular Chemistry, Wiley-VCH, Wienheim*, **1995**.

[26] J. Rebek, *Angew. Chem. Int. Ed., Engl*., **1990**, 29, 245-255.

[27] C. H. Hunter, K. R. Lawson, J. Perkins, C. J. Urch, *J. Chem. Soc., Perkin Trans.* **2001**, 2, 651-699.

[28] M. Nishio, M. Hirota, Y. Umezawa, *The CH-π Interactions, Wiley-VCH, NewYork*, **1998**.

[29] G. M. Whitesides, B. Grzybowski, *Science*, 295, 2418.

[30] M. Dubey, S. L. Bernasek, J. Schwartz, *J. Am. Chem. Soc. **2007**, 129, 6980–6981.*

[31] S. Zhang, C. M. Cardona, L. Echegoyen, *Chem.Commun.* **2006**, 4461–4473.

[32] A. Facchetti, E. Annoni, L. Beverina, M. Morone, P. Zhu, T. J. Marks, G. A. Pagani, *Nat. Mater.* **2004**, 3, 910–917.

[33] Z. Liu, A. A. Yasseri, J. S. Lindsey, D. F. Bocian, *Science* **2003**, 302, 1543– 1545.

[34] M. Altman, A. D. Shukla, T. Zubkov, G. Evmenenko, P. Dutta, M. E Van der Boom, *J. Am. Chem.Soc.* **2006**, 128, 7374–7382.

[35] T. Gupta, M. E. Van der Boom, *J. Am.Chem. Soc.* **2006**, 128, 8400–8401.

[36] A. B. Descalzo, R. Martìnez-Màòez, F. Sancenòn, K. Hoffmann, K. Rurack, *Angew. Chem., Int. Ed.* **2006**, 45, 5924–5948.

[37] C. Lagrost, G. Alcaraz, J.-F. Bergamini, B. Fabre, I.Serbanescu, *Chem. Commun.* **2007**, 1050–1052.

[38] M. Tonezzer, M. Melegari, G. Maggioni, R. Milan, G. DellaMea, E. Dalcanale, *Chem. Mater.* **2008**, 20, 6535–6542.

[39] Crane, R. A. & Scott, T. B. Nanoscale zero-valent iron: Future prospects for an emerging water treatment technology. *J. Hazard. Mater.* 211–212, 112–125 (**2012**).

[40] R. S. Dhanikula, A. Argaw, J. Bouchard, P. Hildgen, *Mol. Pharm.* **2008**, 5, 105.

[41] P. Blasi, S. Giovagnoli, A. Schoubben, M. Ricci, C. Rossi, *Adv. Drug Delivery Rev.* **2007**, 59, 454.

[42] Vlerken, L. E. V.; Vyas, T. K.; Amiji, M. M. *Poly(Ethylene Glycol)-Modified Nanocarriers for Tumor-Targeted and Intracellular Delivery. Pharm. Res.* **2007**, 24, 1405–1414.

[43] Gullotti, E. & Yeo, Y. *Extracellularly activated nanocarriers: A new paradigm of tumor targeted drug delivery. Mol. Pharm.* 6, 1041–1051 (**2009**).

[44] Galvin, P. et al. *Nanoparticle-based drug delivery: Case studies for cancer and cardiovascular applications. Cell. Mol. Life Sci.* 69, 389–404 (**2012**).

[45] Moran, J. R., Karbach, S. & Cram, D. J. Cavitands: synthetic molecular vessels. *J. Am. Chem. Soc.* 104, 5826–5828 (**1982**).

[46] D. J. Cram, S. Karbach, H.-E. Kim, C. B. Knobler, E. F. Maverick, J. L. Ericson, R. C. Helgeson, *J. Am. Chem. Soc.* **1988**, 110, 2229-2237.

[47] a) J. A. Tucker, C. B. Knobler, K. N. Trueblood, D. J. Cram, *J. Am. Chem. Soc.* 1989, 111, 3688-3699. b) P. Soncini, S. Bonsignore, E. Dalcanale, F. Ugozzoli, *J. Org. Chem.* 1992, 57, 4608-4612. c) T. Haino, D. M. Rudkevich, A. Shivanyuk, K. Rissanen, J. Rebek, Jr., *Chem. Eur. J.* 2000, 6, 3797-3805. d) K. Paek, J. Cho, *Tetrahedron Lett.* **2001**, 42, 1927-1929.

[48] A. Friggeri, F.C.J.M. Van Veggel, D.N. Reinhoudt, *Langmuir* **1998**, 14, 5457-5463.

[49] P. Timmerman, W. Verboom, D. N. Reinhoudt, *Tetrahedron* **1996**, 52, 2663.

[50] R. Boukherroub, S. Morin, D. D. M. Wayner, F. Bensebaa, G. I. Sproule, J.-M. Baribeau, D. J. Lockwood, *Chem. Mater.* 2001, 13, **2002**.

[51] a) J.A. Bryant, J.L Ericson, D.J. Cram J. Am. Chem. Soc. 1990, 112, 1255; b) D.J. Cram, H.–J. Choi, J.A. Bryant, C.B. Knobler, *J. Am. Chem. Soc,* **1992**, 114, 7748

[52] P. Roncucci, L. Pirondini, G. Paderni, C. Massera, E. Dalcanale, V.A. Azov, F. Diederich, *Chem. Eur. J.* **2006**, 12, 4775.

[53] E. Dalcanale, P. Soncini, G. Bacchilega, F. Ugozzoli, *J. Chem. Soc. Chem., Chem. Commun* **1989**, 500.

[54] K. D. Stewart, *Ph.D. Dissertation, University of California, Los Angeles,* **1984**.

[55] J. J. Lundquist, T. E. Toone, *The Cluster Glycoside Effect, Chem. Rev.* **2002**, 102, 555-578.

[56] A. G. Cullis, L. T. Canham and P. D. J. Calcott*, J. Appl. Phys*., **1997**, 82, 909.

Chapter 2: Cavitand monolayers on metal oxides for environmental control: VOC detection on functionalized ZnO nanostructures

In this chapter the strategy for the fabrication of a hierarchical hybrid inorganic-organic system suited for the recognition of aromatic volatile organic compounds (VOC) on brush-like ZnO fibers is described. The hybrid material was obtained by a multi-step approach based on the growth of ZnO nanorods onto electrospun ZnO fibers. The ZnO nanostructures were functionalized through the grafting of a bifunctional phosphonic linker (12-azidodecylphosphonic acid) followed by the anchoring of a specific cavitand receptor. The linker was anchored on ZnO fibers through the phosphonic group whilst the azide terminations reacted with a quinoxaline-bridged cavitand (QxCav) having four alkyne groups via "click" reaction. Each reaction step was monitored by using XPS, FTIR and SEM. The recognition properties of this hybrid nanostructures towards α,α,α,-trifluorotoluene (TFT) vapors

were evaluated by XPS and Raman measurements. The obtained results confirmed the success of the overall synthetic approach which combines the recognition molecular properties of cavitand receptor with the peculiar characteristics of the brush-like ZnO nanostructure.

2.1 Introduction

ZnO is a very interesting material with unique physical and chemical properties, such as optical and electrical features and furthermore is nontoxic, inexpensive and has a high chemical stability. It is classified as a direct wide band gap semiconductor (3.37 eV at room temperature) and for this reason is one of the most promising materials for the fabrication of optoelectronic and gas sensing devices. Moreover, the possibility to easily built nanostructure from this material paves the way for the study of new properties that depend on shape and size.

Zinc oxide can occur in one- (1D), two- (2D) and three-dimensional structures. One-dimensional structures gather the largest group, including nanorods, -needles, -helixes, -springs

and -rings, -ribbons, -tubes, -belts, -wires and -combs. Nanoplates/nanosheets and nanopellets make up the 2D structures whereas examples of 3D structure include flowers, dandelions, snowflakes, etc. To date all those structures have been successfully synthesized but, as said before, one-dimensional nanostructures have caught researchers' attention because of their wide range of potential applications.

With regard to 1D Zinc oxide, in the past years those nanostructures have been prepared by various method such as thermal evaporation, chemical vapour deposition (CVD), vapour-liquid-solid (VLS), metal organic vapour deposition (MOCVD), arc discharge and laser ablation.

2.2 Molecular recognition of aromatic volatile organic compounds (VOCs)

Increased Volatile Organic Compounds (VOCs) emissions' level and their impact on air quality is nowadays considered one of the most important environmental concern. [1-2] Those compounds are man-made or naturally occurring highly reactive hydrocarbons. Natural origins of VOCs include

wetlands, forests, oceans and volcanoes but the majority of them are created from anthropogenic activities consisting of manufacturing or petrochemical industries and vehicular emissions. Indeed, some VOCs are well-known as highly toxic or carcinogenic in nature and may cause both short- and long-term impacts on human health as well as on the natural ecosystem. [3-4] For example, the benzene has a high potential to damage humans in both specific (e.g., the stomach, kidneys, liver and spleen) and systematically (e.g., the nervous, reproductive, circulatory, immune, cardiovascular and respiratory systems) ways. Consequently, a number of major environmental safety agencies (e.g., National Institute of Occupational Safety and Health (NIOSH), Environmental Protection Agency (EPA), and European Agency for Safety and Health at Work (EU-OSHA)) have established guidelines to limit the exposure of humans to VOCs in indoor and workplace air in light of their effects on health. Furthermore, VOCs are known to be precursors of tropospheric ozone and for this reason, their emissions are limited by legislation in many regions so the detection and quantification of these molecules is critical. Highly sensitive analytical techniques (including chromatography, mass spectrometry, nuclear

magnetic resonance, etc.) have commonly been employed for the accurate quantification of VOCs. However, these techniques display some drawbacks (e.g. high expenses, lack of portability, etc.), that constitutes a barrier for their use in everyday analysis. Moreover, such techniques often require complex and time consuming pre-treatment steps. Among alternatives, many sensor-based systems have been explored; using a wide range of detection principles, such as semiconducting metal oxides, conductive polymers, quartz crystal microbalance sensors and electronic nose, it is possible to achieve cheaper and compact devices. Nonetheless, such sensors generally suffer from sensitivity, selectivity and stability limitation. In this scenario I have investigated the possibility to modify such magnetic nanoparticles' surface in order to decrease those limitations using specific molecules anchored by a multistep approach.

2.3 General Procedures

2.3.1 ZnO brush-like nanofibers preparation

A solution containing 2.7 g of PVP and 0.9 g of $Zn(CH_3COO)_2 \cdot 2H_2O$ in 9.5 mL of DMF was electrospun using

a commercial electrospinning system (EC-DIG Electrospinning, IME Technologies). The polymeric solution was stirred for 4 hours and loaded in a 5 mL plastic syringe tipped by a stainless steel needle. The solution was delivered using a flow rate of 5 μL/min. Electrospinning was carried out in ambient conditions (temperature 21 °C) and controlled relative humidity (40%). A positive bias of +19 kV was applied to the spinneret by a high voltage power supply. Silicon substrate were placed on a metallic collector and biased at -4 kV (distance needle - collector 16 cm). The electrical field applied to the drop formed at end of a syringe's needle produced the nanofibers that were collected on the surface of the silicon substrates.

The Zn doped PVP nanofibers are used as template for deposition of a ZnO seed layer by MOCVD (Metal Organic Chemical Vapor Deposition). Deposition of ZnO seed layer was performed in a hot wall tubular reactor using a diamine (N,N,N,N′-tetramethylethylendiamine) (TMEDA) adduct of Zinc(II)bis(2-thenoyl-trifluoroacetonate) [Zn(tta) 2•tmeda].[5] A slow temperature ramp up (5°C/min) was set to reach the deposition temperature (500°C) and deposition time was set at 45 min. Ar (250 sccm) and O_2 (250 sccm) have been used as

carrier and reactive gas respectively. Pressure during deposition is ~2 Torr. Polymeric component is burned during seed layer deposition thus forming ZnO nanofibers on which the MOCVD seed layer was deposited. An external shell of ZnO nanorods is grown all around these nanofibers by Chemical Bath Deposition at atmospheric pressure and 80°C. Substrates were dipped face down in a nutrient bath containing a 0,025 M aqueous solution of zinc acetate dehydrate and ethylenediamine (EDA) and kept under mild stirring at 80°C for 6 hrs.[5] After CBD growth substrates were sonicated in water for 1 minute to remove the ZnO microrods genereted in solution from homogeneous growth.[6]

The procedure above described used to prepare ZnO brush-like fibers (bare ZnO fibers) which combines MOCVD and CBD (Chemical Bath Deposition) processes.[5] has been monitored step by step through SEM analysis performed with LEO SUPRA 55VP equipped with a field emission gun. Figure 2.1a shows PVP electrospun nanofibers after ZnO seed layer deposition by MOCVD. After a slow temperature ramp up (from room temperature to deposition temperature set at 500°C), the polymer is degraded and the remaining ZnO fibers[7] act as scaffold for the following CBD process to grow

a brush-like ZnO nanorods external shell (Figure 2.1b). SEM image clearly evidences the morphological evolution of these hierarchically ZnO based structures from nanofiber mats to microsized tubular ZnO brushes, resulting from high density growth of ZnO nanorods. By comparing the fibre size in Figure 2.1a (~200 nm) and 1b (~2 μm) the estimated maximum length of ZnO nanorods is about 800 nm.

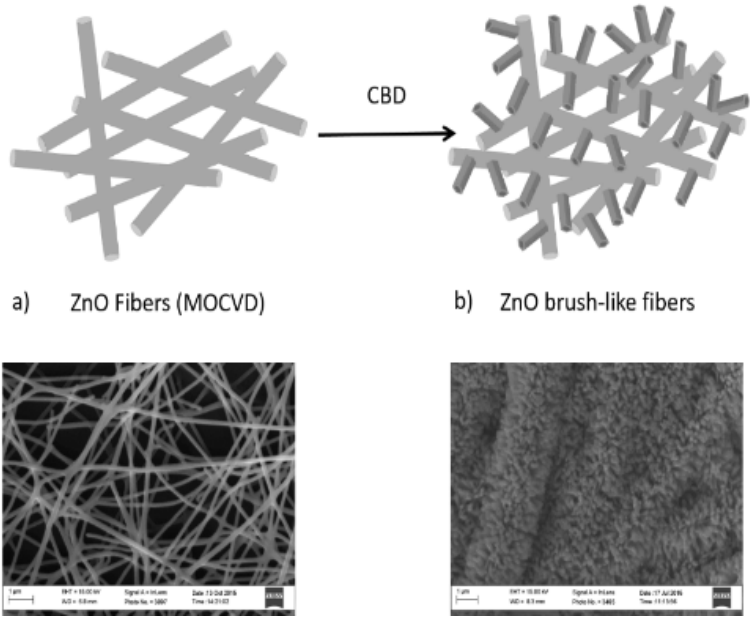

Figure 2. 1: Schematic representation of hierarchical ZnO fibers synthesis: a) ZnO fibers deposited by MOCVD onto Zn doped PVP electrospun nanofibers, b) brush-like ZnO nanorods grown by CBD

2.3.2 QxCav Synthesis

The synthesis of functional molecule to fix onto the nanostructured ZnO surface was carried out at the **University of Parma** by the research group of **Prof. E. Dalcanale** according the two steps pathway shown in Figure 2.2.

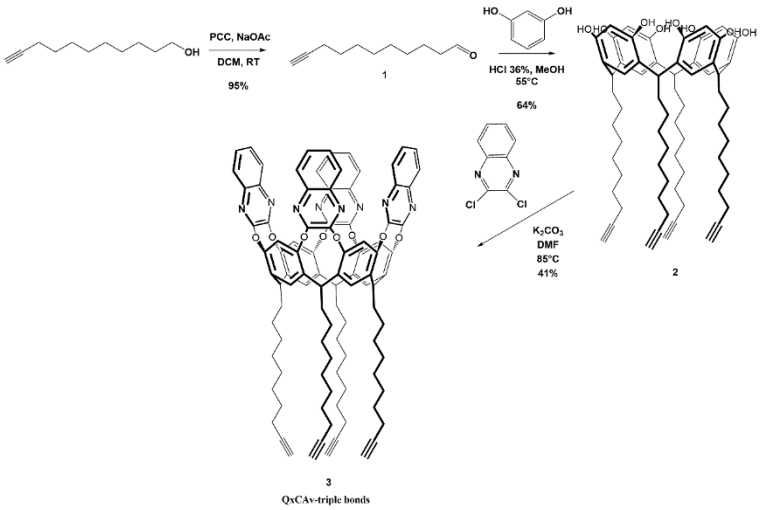

Figure 2. 2: Synthetic scheme for QxCav 3 with four ω-triple bonds at the lower rim.

The first step is the synthesis of resorcinarene that was performed adding 1.53 g, $9.3 \cdot 10^{-3}$ mol, of aldehyde **1** (synthesized according to literature procedure[8]) to a stirred solution of resorcinol (1.01 g, $9.1 \cdot 10^{-3}$ mol) in methanol (70

mL) cooled to 0 °C, then 5.0 mL of HCl 36% was added dropwise. After 4 days of stirring at 55 °C, the mixture was allowed to cool to room temperature and poured into distilled water (450 mL). A precipitate formed, which was filtered, dried under vacuum and recrystallized from MeOH to give product **2** as a yellow pale solid (1.5 g, 64% yield). The product was then characterized by ^{1}H NMR and ESI-MS and the results are shown below:

^{1}H NMR (400 MHz, 298 K, DMSO-d_6): δ (ppm) 8.87 (s, 8H, Ar***OH***); 7.16 (s, 4H, Ar***H***); 6.14 (s, 4H, Ar***H***) 4.21 (t, J = 7.6 Hz, 4H, Ar***CH***); 2.69 (t, J = 2.6 Hz, 4H, CC***H***); 2.14 - 2.09 (m, 8H, CHC***CH$_2$***); 2.07 – 1.90 (m, 8 H, CH***CH$_2$***CH_2); 1.50 – 1.10 (m, 48H, CH_2).

ORBITRAP-ESI-MS: m/z calculated for $C_{68}H_{87}O_8$ $^{[}$M-H$^{]-}$: 1031.6401. Found: 1031.6402 $^{[}$M-H$^{]-}$

The second step consists of tying up quinoxalinic groups on resorcinarene structure. To do this 0.6 g of K_2CO_3 ($4.0 \cdot 10^{-3}$ mol) was added to a solution made of 0.3 g resorcinarene **2** ($2.9 \cdot 10^{-4}$ mol) in 20 mL of dry DMF; the mixture was stirred at room temperature. After 15 minutes, 2,3-dichloroquinoxaline (0.2 g, $1.13 \cdot 10^{-3}$ mol) was added and the reaction was further

stirred for 12 h at 85 °C. The reaction mixture was cooled to room temperature and quenched pouring it into 20 mL of 1N HCl solution. The resulting precipitate was recovered, washed with water and dried. The crude was purified thought flash chromatography (SiO_2, CH_2Cl_2/EtAc 97/3) and recovered as light yellow solid (0.6 g, 41% yield).

The product was then characterized by ^1H NMR and HR-MALDI-TOF and the results are shown below:

^1H NMR (400 MHz, 298 K, $CDCl_3$,) δ= 8.18 (s, 4H, Ar***H***); 7.83-7.80 (m, 8H, Ar***H***, part AA' of an AA'BB' system); 7.51-7.49 (m, 8H, Ar***H***, part BB' of an AA'BB' system); 7.20 (s, 4H, Ar***H***); 5.60 (t, J = 8.0 Hz, 4H, Ar***CH***); 2.30 - 2.21 (m, 16H, CHC***CH_2*** + CH***CH_2***CH_2); 1.99 (t, J = 2.5 Hz, 4H, CC***H***); 1.62 – 1.35 (m, 56H, CH_2).

HR-MALDI-TOF: m/z calculated for $C_{100}H_{97}N_8O_8$ $^{[}MH^{]+}$: 1537,7429. Found: 1537.942 $^{[}MH^{]+}$

2.3.3 N_3-PA functionalized ZnO nanofibers

The ZnO brushes fibers were further functionalized by a multi-step approach shown in Figure 2.3. The first step consists on the grafting of a phosphonic acid, bearing a terminal azide group, 12-azidododecylphosphonic acid (N_3-PA). Thanks to

phosphonic group the linker was covalently grafted onto the bare ZnO nanofibers, forming a monolayer (N_3-PA@ZnO) through P–O–Zn [9] bonds.

The ZnO nanofibers were reacted using the droplet method[10-11], in order to avoid any degradation of the morphology of the fibers, with 10 mM N_3-PA solution in 2:1 1-butanol/ethanol for 5 hours, then rinsed thoroughly with neat solvent and dried under nitrogen flow.

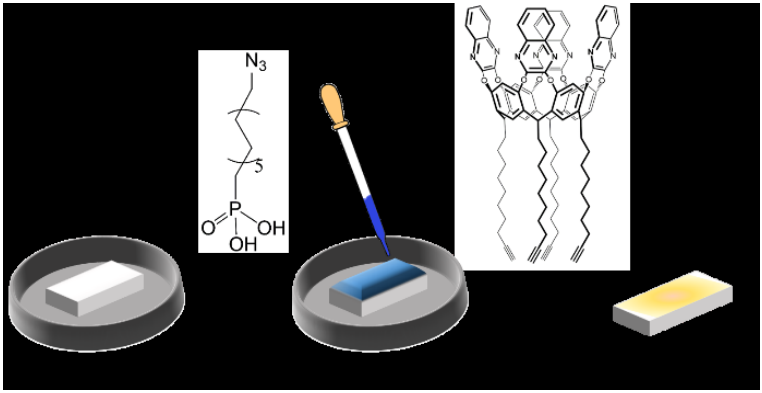

Figure 2. 3: Reaction steps for the preparation of functionalized ZnO fibers.

2.3.4 QxCav click reaction

These QxCav molecules bearing four terminal acetylenic groups were then covalented bonded on the functionalized fiber *via* a click chemisty reaction. N_3-PA@ZnO sample was dipped in a solution containing $CuSO_4$ (0.01 mmol) and (+)-sodium L-

ascorbate (0.05 mmol) in THF(10 ml). The reaction was accomplished at 25 °C for 5 hours. The sample was then removed from the solution, washed with THF, three times, and dried under nitrogen flow. After click-chemistry, the surface shows a negligible degradation and morphology remains almost unchanged, as shown in Figure 2.4, where the hierarchical brush structure of fibres is well discernible (circled insert).

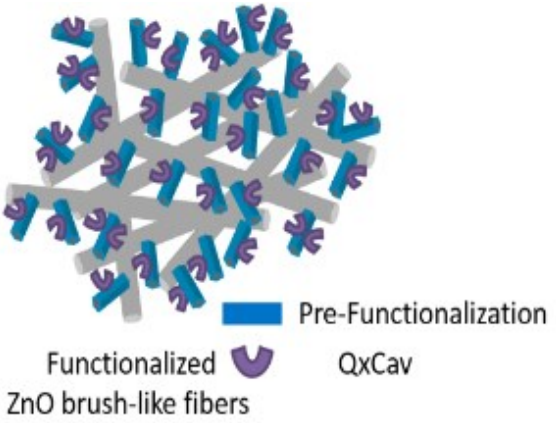

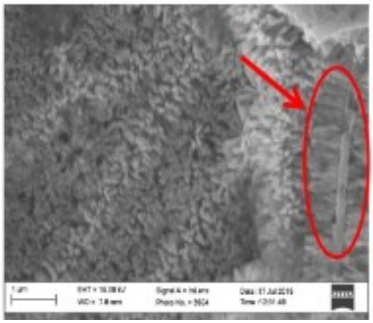

Figure 2. 4:brush-like ZnO nanorods after click reaction.

2.4 Sample characterization

XPS spectra were run with a PHI 5600 multi-technique ESCA-Auger spectrometer equipped with a monochromated Mg *K* X-ray source. Analyses were carried out with a photoelectron angle of 45° (relative to the sample surface) with an acceptance angle of ± 7°. The XPS binding energy (B.E) scale was calibrated by centering the C 1s peak due to hydrocarbon moieties and "adventitious" carbon at 285.0 eV.[12] SEM analysis was performing with a LEO SUPRA 55VP equipped with a field emission gun. Transmission FTIR measurements were recorded on a JASCO FT-IR 430, with 100 scans collected per spectrum (scan range 400-4000 cm^{-1}, resolution 4 cm^{-1}). X-Ray powder diffraction (XRD) measurements were performed with a θ-θ 5005 Bruker-AXS diffractometer (Zeiss, Oberkochen, Germany) using Cu Kα radiation operating at 40 kV and 30 mA.

Raman spectra have been taken by using a Witec Alpha 300 spectrometer. Acquisition were performed with a Nd:YAG 532

nm laser exiting radiation radiation with power densites below 1 mW to avoid heating effects.

2.4.1 XRD characterization

XRD measurements reported in Figure 2.5 clearly indicate the crystalline nature of these ZnO brushes and, accordingly, the typical diffraction pattern of wurtzite crystal structure (JCPDSC 36-1451) is detected either after MOCVD seeding process (red line) and after CBD nanorods growth (green line).

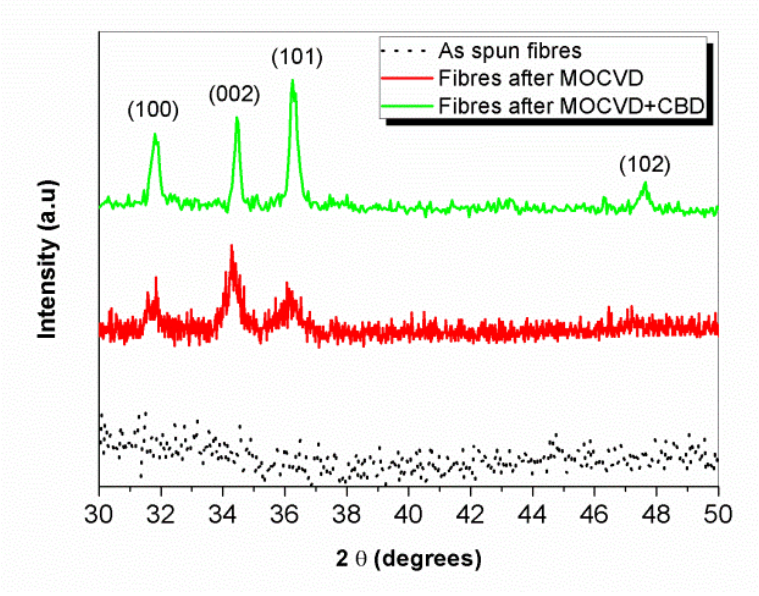

Figure 2. 5: XRD patterns diffraction of as spun fibres (black line), fibres after MOCVD (red line) and fibres after MOCVD + CBD (green line).

Noteworthy, the expected texturing along the (002) plane cannot be detected,[13] due to the brush-like structure of the sample. However, it is clear from the detail in the insert of Figure 2.4 that ZnO nanorods grow perpendicularly and well aligned all around the tubular ZnO nanofibers surface.

2.4.2 FT-IR characterization

All ZnO nanofibers, bare ZnO fibers, N_3-PA@ZnO and QxCav-N_3-PA@ZnO have been characterized by FT-IR and XPS. Figure 4 shows the FTIR spectra comparison of bare ZnO fibers, N_3-PA@ZnO and QxCav-N_3-PA@ZnO. In particular, two spectral regions are reported: (a) the C–H stretching region between 3200 and 2800 cm^{-1} and (b) the N_3 – alkyne stretching region between 2200 and 2000 cm^{-1}. The spectra in the 2200 and 2000 cm^{-1} region show for both N_3-PA@ZnO and QxCav-N_3-PA@ZnO a band at 2120 cm^{-1} absent in the spectra of bare ZnO. In the case of N_3-PA@ZnO, this feature is clearly related to the characteristic absorption peak of the azide group, thus suggesting that the anchoring process preserves the active groups. After the click reaction, the decreasing of the azide band in QxCav-N_3-PA@ZnO spectra indicates the proceeding of the “click reaction” which lead the transformation of azide

group to triazole. Note in addition that the further broadening of the band is due to the stretching of C≡C group of un-reacted termination of the bonded QxCav molecules. The C-H stretching region between 2800–3200 cm^{-1} shows for N_3-PA@ZnO the appearance of C-H stretches compared to the bare ZnO. However, a significant increase in intensity of CH_2 stretching at 2930 and 2850 cm^{-1} is observed in the spectra of QxCav-N_3-PA@ZnO, compared to N_3-PA@Zn, reflecting the increased number of CH_2 groups related to the presence of the QxCav alkyl chains. In addition, the surface anchoring of QxCav is confirmed by the presence of the peak at 3060 cm^{-1} in the QxCav-N_3-PA@ZnO sample, diagnostic of the stretches of aromatic C−H (ν(CH)).[14-15]

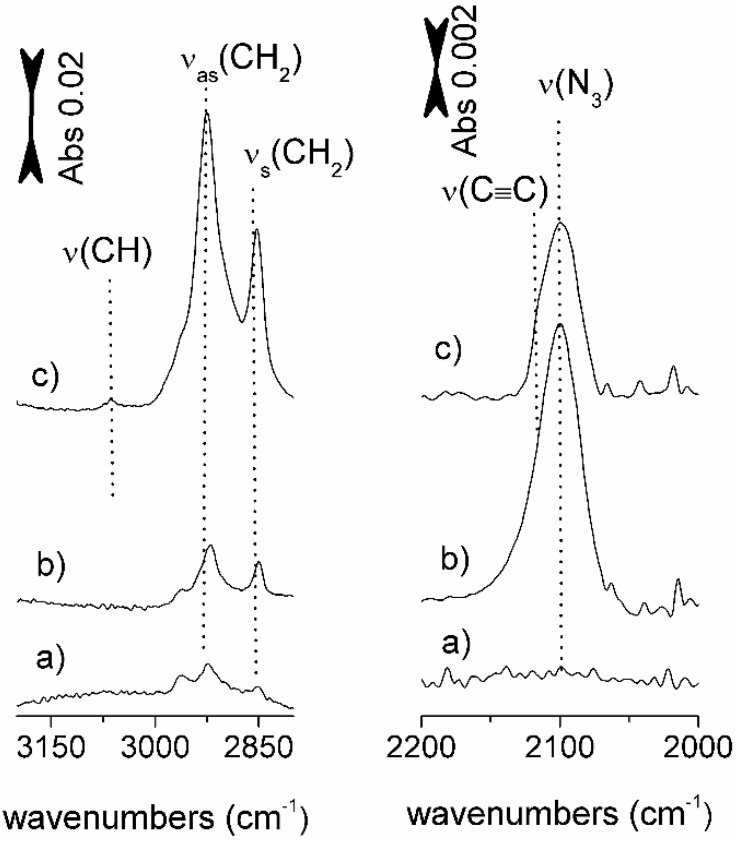

Figure 2. 6: FT-IR spectral regions in the 3200–2800 cm^{-1} (left) and 2200–2000 cm^{-1} (right) ranges of a) bare ZnO fibers, b) N_3-PA@ZnO and c) QxCav-N_3-PA@ZnO

2.4.3 XPS characterization

XPS characterization also gives further indication on the success of the anchoring process. XPS P2p and N1s spectral

regions of bare ZnO, N_3-PA@ZnO and QxCav-N_3-PA@ZnO samples are shown in Figure 2.7. The presence and the position of the P2p band is a reliable indicator to evaluate the phosphonic acid grafting process. The P2p peak of N_3-PA@ZnO (absent in the bare ZnO nanofibers) is observed at 133.2 eV: this value is typical of phosphonic acids on transition metal oxide surfaces anchored in a bidentate way.[16]After QxCav grafting, the P2p band of QxCav-N_3-PA@ZnO is still centred at 133.2 eV, thus indicating that the anchored phosphonic acid is not removed by the click reaction. As expected, bare ZnO nanofibers do not show any signal in the N1s spectral region whereas in the N_3-PA@ZnO sample, two N1s bands are observed: a main broad band around at 400.8 eV and a lower peak at 405.1 eV. The latter can be associated to the positively charged N atom of the $–N=N^+=N^-$ azide resonance structure, while the envelope around 400.8 eV is due to the convolution of neutral and negatively charged N atoms.[17] Note that the intensity of the component at about 405.1eV decrease after prolonged XPS irradiation. After QxCav grafting, the N1s peak was observed at 399.8 eV, shifted towards lower binding energies (B.E.). The observed B.E. value is consistent with the presence of the quinoxalinic

ring nitrogen's atoms. Moreover, the signal corresponding to electron deficient N atom of the azido group at 405.1 eV disappeared, indicating that the azide group is consumed in the formation of the triazolic ring, whose signal at 401.0 eV[17-18] is superimposed with the broad band centred at 399.8 eV.

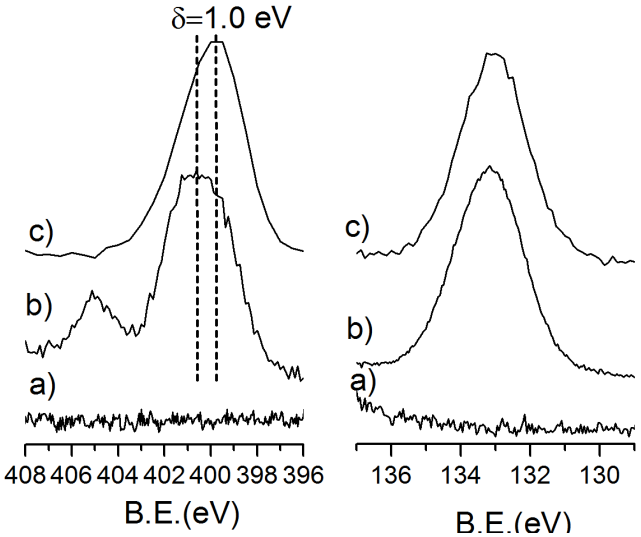

Figure 2. 7: High resolution N1s (left) and P2p (right) XPS spectral regions of a) bare ZnO, b) N_3-PA@ZnO and c) QxCav-N_3-PA@ZnO

2.5 Sensing Test

Gas−solid complexation tests were performed exposing QxCav-N_3-PA@ZnO and N_3-PA@ZnO (as inactive reference) to vapours of α,α,α-trifluorotoluene (TFT) and evaluated by XPS and Raman spectroscopies. The TFT guest was chosen as

fluorine-marked compound to test the affinity of decorated-surfaces towards aromatic VOCs. The presence of the F1s band in the XPS spectra of QxCav-N_3-PA@ZnO (Figure 2.8) after exposure to the TFT vapours proved the complexation capability of the cavitand-functionalized surface. The absence of the halogen signals on N_3-PA@ZnO (Figure 2.8) rules out the possibility of physisorption due to unspecific interactions between the guest and the ZnO surface.

Raman spectra are reported in Figure 2.9 and validate the successful use of the functionalized ZnO brushes to detect aromatic compound, as TFT. The Qx-Cav and TFT main Raman peaks are reported for comparison.

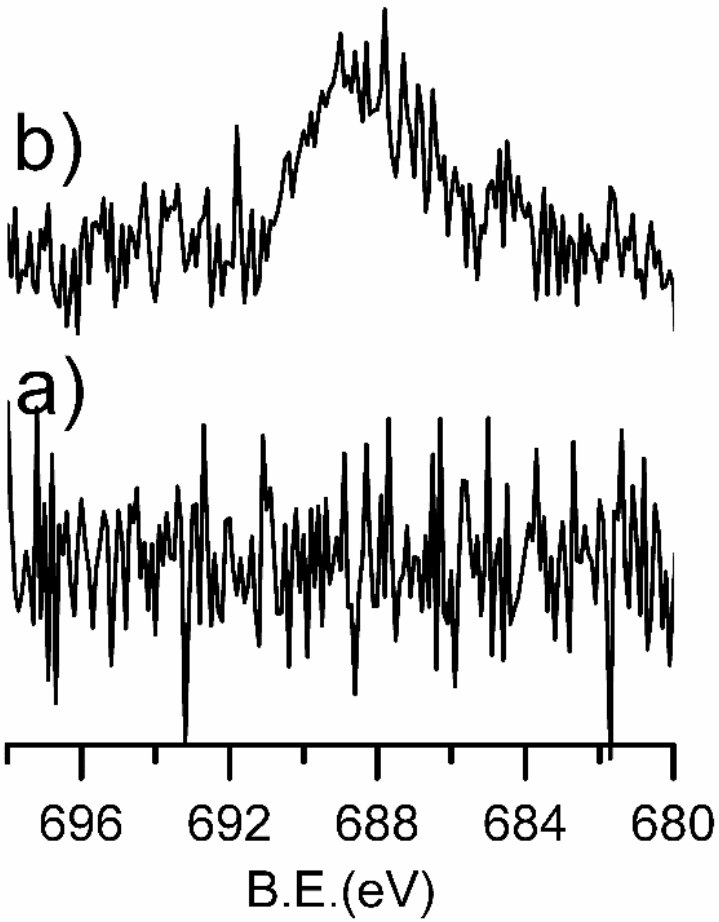

Figure 2. 8: F1s spectral regions of a) N_3-PA@ZnO and b) QxCav-N_3-PA@ZnO after exposure to TFT vapours.

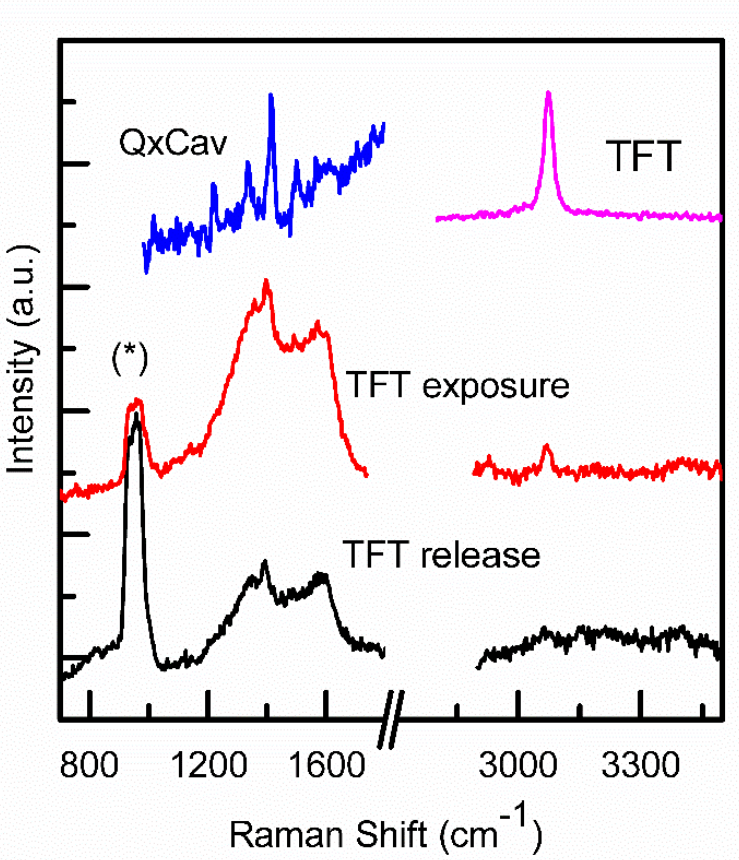

Figure 2. 9: Raman Spectra of QxCav-N₃-PA@ZnO after exposure to TFT vapours (red lines) and after TFT release (black lines). QxCav (blue line) and TFT (magenta line) compounds were added as reference.

The spectra display several active modes, attributed to both Si substrate, ZnO brushes, linked cavitand and TFT analyte. Accordingly, Raman spectra of bare QxCav and TFT (dropped

on silicon) are reported for comparison. The recorded spectra exhibit two main characteristic bands in the spectral region between 1000 and 2000 cm^{-1}: the first order G mode (E2g symmetry) at ~1600 cm^{-1} is attributed to sp2 graphitic network, while the D mode (A1g symmetry) at ~ 1350 cm^{-1} reflects the disorder and defects in the carbon lattice. The presence of these bands is due to carbonaceous residues of thermal degradation of PVP during MOCVD seed deposition. The sharp peak at about 1400 cm^{-1} is attributed to C-H bending mode of grafted cavitand while the one at 3070 cm^{-1} belongs to C-H stretching of analyte. After exposure to TFT atmosphere, the peak at 3070 cm^{-1} appeared in the Raman specrum of the material. Noteworthy, this last signal disappears after desorption of TFT out from functionalized ZnO brush-like nanofibers, performed by flowing warm N_2 for 15 minutes.

2.6 Conclusions

In this chapter, I reported on the synthesis and characterization of a new sequentially-grown nanostructured material consisting of brush-like ZnO nanofibers covalently functionalized with cavitand receptors. The brush-like structure was obtained

performing MOCVD and CBD processes on electrospun ZnO nanofibers used as substrate for column growth. The columnar nanostructures were coated with an azidophosphonic acid monolayer, which acts as linker for the anchoring of a QxCav receptor functionalized at the lower rim with 4 terminal alkyne moieties. The efficiency of the grafting methodology was monitored by SEM, FT-IR and XPS. The hierarchical structure of the obtained material, whose morphology is not affected by the functionalization routes, is clearly shown by SEM analysis. FT-IR and XPS indicate that the phosphonic linker is covalently bound to the surface leaving N_3 groups intact and suited for receptor anchoring. QxCav is grafted to the monolayer coated nanostructure via click-reaction. The reaction evolution was monitored through the consumption of N_3 groups, shown by the decrease of azide related FT-IR and XPS signals.

Gas-solid complexation tests were monitored through complementary techniques, namely surface sensitive XPS and bulk Raman spectroscopy. Results indicate that the inherent recognition properties of the QxCav receptors towards aromatic analytes are retained after their anchoring, showing that this is a suitable way to convey recognition properties to

organized nanostructured materials. Further studies must be performed to optimized the signal transduction even though the Raman spectroscopy could be easily performed.

---

[1] Stebounova LV, Morgan H, Grassian VH, Brenner S. *Health and safety implications of occupational exposure to engineered nanomaterials. Wiley Interdiscip Rev. Nanomed. Nanobiotechnol.* **2012**; 4:310–21.

[2] Ashford NA, Caldart CC. *Government regulation of environmental and occupational health and safety in the United States and the European Union. In: Levy BS, Wegman DH, Sokas R, Baron S, editors. Occupational and environmental health: recognizing and prevent- ing disease and injury. 6th ed. Oxford UK: Oxford University Press;* **2010**. p. 640–63.

[3] Atkinson R. *Atmospheric chemistry of VOCs and NOx . Atmos Envi- ron* **2000**; 34:2063–101.

[4] Kim KH, Jahan SA, Kabir E. *A review of breath analysis for diagnosis of human health. Trends Anal Chem* **2012**; 33:1–8.

[5] Fragalà, M. E.; Aleeva, Y.; Malandrino, G. *Effects of Metal-Organic Chemical Vapour Deposition grown seed layer on the fabrication of well aligned ZnO nanorods by Chemical Bath Deposition. Thin Solid Films* **2011**, 519, 7694-7701.

[6] Fragalà, M. E.; Aleeva, Y.; Malandrino, G. *ZnO nanorod arrays fabrication via chemical bath deposition: Ligand concentration effect study. Superlattices and Microstructures* **2010**, 48, 408-415.

[7] Di Mauro, A.; Zimbone, M.; Scuderi, M.; Nicotra, G.; Fragalà, M. E.; Impellizzeri, G. *Effect of Pt Nanoparticles on the Photocatalytic Activity of ZnO Nanofibers. Nanoscale Res Lett.* **2015**, 10, 484-490.

[8] Cheng, X.; Li, L.; Uttamchandan, M.; Yao, S. Q. *In Situ Proteome Profiling of C75, a Covalent Bioactive Compound with Potential Anticancer Activities. Org. Lett.* **2014**, 16, 1414−1417.

[9] Smecca, E.; Motta, A.; Fragalà, M. E.; Aleeva, Y.; Condorelli, G. G. *Spectroscopic and Theoretical Study of the Grafting Modes of Phosphonic Acids on ZnO Nanorods. J. Phys. Chem. C* **2013**, 117, 5364−5372.

[10] Wang, X.; Liu, L.; Luo, Y.; Zhao, H. *Bioconjugation of Biotin to the Interfaces of Polymeric Micelles via In Situ Click Chemistry. Langmuir* **2009**, 25, 744−750.

[11] Cao, Y.; Galoppini, E.; Reyes, P. I.; Lu, Y. *Functionalization of Nanostructured ZnO Films by Copper-Free Click Reaction. Langmuir* **2013**, 29, 7768−7775.

[12] a) I. L. Swift, *Surf. Interface Anal.* **1982**, 4, 47–51. *b)* D. Briggs, G. *Beamson, Anal. Chem.* **1992**, 64, 1729–1736.

[13] Fragalà, M. E.; Di Mauro, A.; Litrico, G.; Grassia, F.; Malandrino G.; Foti G. *Controlled large-scale fabrication of sea sponge-like ZnO nanoarchitectures on textured silicon. CrystEngComm* **2009**, 11, 2770–2775.

[14] Tudisco, C.; Betti, P.; Motta, A.; Pinalli, R.; Bombaci, L.; Dalcanale, E.; Condorelli, G. G. *Cavitand-Functionalized Porous Silicon as an Active Surface for Organophosphorus Vapor Detection. Langmuir* **2012**, 28, 1782−1789.

[15] Friggeri, A.; van Veggel, F. C. J. M.; Reinhoudt, D. N. Self-Assembled *Monolayers of Cavitand Receptors for the Binding of Neutral Molecules in Water. Langmuir* **1998**, 14, 5457−5463.

[16] Tudisco, C.; Oliveri, V.; Cantarella, M.; Vecchio, G.; Condorelli, G. G. *Cyclodextrin Anchoring on Magnetic Fe3O4 Nanoparticles Modified with Phosphonic Linkers. Eur. J. Inorg. Chem.* **2012**, 5323–5331.

[17] Gouget-Laemmel, A. C.; Yang, J.; Lodhi M. A.; Siriwardena, A.; Aureau, D.; Boukherroub, R.; Chazalviel, J.-N.; Ozanam, F.; Szunerits S. *Functionalization of Azide-Terminated Silicon Surfaces with Glycans Using Click Chemistry: XPS and FTIR Study. J. Phys. Chem. C* **2013**, 117, 368−375.

[18] Li, Y.; Wang, J.; Cai, C. Z. *Rapid Grafting of Azido-Labeled Oligo(ethylene glycol)s onto an Alkynyl-Terminated Monolayer on*

Nonoxidized Silicon via Microwave-Assisted "Click" Reaction. Langmuir **2011**, 27, 2437−2445.

Chapter 3: Cavitand monolayers on metal oxides for environmental control: functionalized magnetic nanoparticles for water purification

In this chapter, a different pathway was carried out to functionalized MNPs with a mixture of phosphonic acids bearing azido and amino terminal groups, respectively. Using those two terminal groups it is possible to anchor a quinoxaline cavitand receptor (QxCav), bearing four alkyne moieties, on azido groups through a "click-reaction" and, moreover, N-hydroxysuccinimide (NHS) activated forms of poly(ethylene glycol) on the amine terminals by DCC/NHS coupling reactions.

Simultaneously, a different batch of nanoparticles was synthesised following a similar pre-functionalization pathway but using a mixture of alkyne and amino terminated phosphonic acids. Those moieties are suited to anchor a phosphonic bridged cavitand (4PO) bearing an azido

termination through a “click-reaction”, analogues to the previous one, with the alkyne termination of the phosphonic acid and the NHS-activated form of poly(ethylene glycol) onto the surface by DCC/NHS coupling reaction.

Those two decorated nanoparticles thanks to intrinsic magnetic properties of the magnetic core, that allows an easy and rapid removal from aqueous media, and to the QxCav π-π interaction, in the first batch, suited for complexation of aromatic contaminants or 4PO cation-dipole and CH-π interactions, in the second one, suited for complexation of N-methylated comtaminants often encountered in herbicides (paraquat), can be employed for water purification.

3.1 MNPs for the removal of aromatic compounds in water

The alarming lack of drinking water due to the harmful levels of pollutants in there represents a crucial issue worldwide. It is clear that contaminants present in wastewater as heavy metals, inorganic compounds, organic pollutants, etc. worsen human beings’ life and even ecological environment.

It is thus necessary trying to reduce contamination and remove as much as possible those compounds from wastewater in order to obtain drinking water.

Again, nanotechnology represents a true asset to limit this phenomenon, in fact nanomaterials displays unique properties not found in bulk- sized materials that are useful in wastewater treatment. In particular iron oxide nanoparticles can be employed to remove these pollutants because of their intrinsic magnetic properties. Moreover, the modification of this nano-sized systems is a further advantage because of the possibility to engineering the surface with proper molecular building-blocks.

3.2 General Procedure

The overall approach for the synthesis of cavitand-decorated nanosystems is shown in Figure 3.1

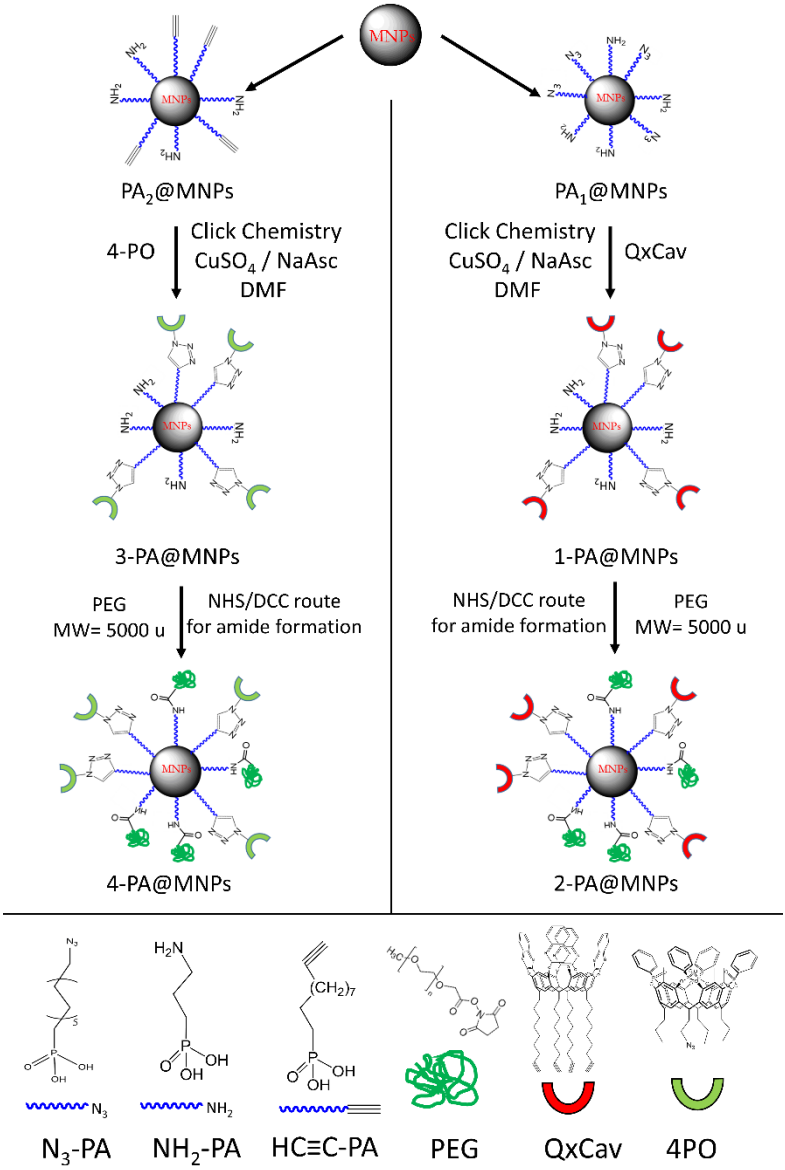

Figure 3. 1: Synthesis of cavitand-decorated nanosystems

3.2.1 Synthesis of Magnetic Iron Oxide nanoparticles (MNPs)

Bare iron oxide nanoparticles were synthesized by alkaline co-precipitation of Fe^{3+} and Fe^{2+} according to the protocol described in the literature.[1] Briefly, $FeCl_2 \cdot 4H_2O$ and $FeCl_3 \cdot 6H_2O$ (molar ratio 1:2) were dissolved in water (50 mL) under a N_2 atmosphere with vigorous stirring. NH_4OH (5 mL, 25%) was added to the solution at 80°C, and the reaction was continued for 30 min. The resulting suspension was cooled to room temperature and washed with ultrapure water. The obtained bare magnetic nanoparticles (bare MNPs) were isolated from the solvent by magnetic decantation.

3.2.2 Synthesis of monoazide tetraphosphonate cavitand (4PO-N_3)

4PO-N_3 was prepared at the **University of Parma** by the research group of **Prof. E. Dalcanale** following a published procedure.[2]

To a solution of monochloro footed tetraphosphonate cavitand (4-PO) (0,44 g, 0.35 mmol) in DMF (15 ml), sodium azide was

added (68 mg, 1.1 mmol). The solution was stirred overnight at 55°C. Then the solvent was evaporated and the crude was suspended in water and filtered affording 4PO-N_3 as a brown solid (0,38 g., 0.31 mmol, 86%). **^{1}H-NMR ($CDCl_3$, 400 MHz)**: δ = 8.14 (m, 8H, P(O)Ar**H$_O$**); 7.65 (m, 4H, P(O)Ar**H$_P$**); 7.57 (m, 8H, P(O)Ar**H$_M$**); 7.19 (s, 4H, Ar**H**); 4.87 (m, 4H, ArC**H**); 3.48 (t, 2H, ^{3}J= 6.2 Hz $CH_2C\mathbf{H_2}N_3$); 2.38 (m, 20H, $C\mathbf{H_2}CH_2CH_2N_3$ + $C\mathbf{H_2}CH_2CH_3$ + Ar$C\mathbf{H_3}$); 1.73 (m, 2H, $CH_2C\mathbf{H_2}CH_2N_3$); 1.47 (m, 6H, $CH_2C\mathbf{H_2}CH_3$); 1.09 (t, 9H, ^{3}J= 7.2 Hz, $CH_2CH_2C\mathbf{H_3}$). **^{31}P{^{1}H} NMR ($CDCl_3$, 161.9 MHz)**: δ = 6.13 (bs P(O)). **HR ESI-MS**: calculated for the complex **4PO[N_3, CH_3, Ph]** $C_{68}H_{67}N_3O_{12}P_4$ (1241.36752) $[M+Na]^+$: 1264.35729. Found:1264.35674.

3.2.3 (PA_1@MNPs & PA_2@MNPs) MNPs functionalization with PAs mixtures

MNPs (300 mg) were dispersed in a mixture of H_2O/DMF 1:1 (25 ml) using an ultrasonic bath for 30 min. 12-azidododecylphosphonic acid (N_3-PA) (109 mg) and 3-aminopropylphosphonic acid (NH_2-PA) (52 mg) were added and the suspension was kept under agitation for 6 h at room

temperature. The particles (PA_1@MNPs) were then magnetically separated and washed three times with reaction mixture followed by water and ethanol and dried under air.

Similarly, another batch of MNPs (300 mg) were dispersed in DMF (25 ml) using an ultrasonic bath for 30 min. A mixture of 10-undecynylphosphonic acid (HC≡C-PA) (100 mg) and 3-aminopropylphosphonic acid (NH_2-PA) (180 mg) was added and the suspension kept under constant agitation for 6 h in order to obtain a different phosphonic monolayer (PA_2@MNPs). The separation and cleaning process of this batch is the same as described for PA_1@MNPs.

3.2.4 (1-PA@MNPs) QxCav anchoring on PA_1@MNPs

PA_1@MNPs (0.2 g) and QxCav (5 mg) were dispersed in DMF (10 mL), then $CuSO_4$ (7.5 mg) and (+)-sodium L-ascorbate (40 mg) were added in sequence. The mixture was vibrated with an orbital shaker at 25 °C for 24 hours.

Afterwards, QxCav functionalized PA_1@MNPs were separated magnetically washed three times with DMF and once with ethanol and at last dried overnight at 25°C.

3.2.5 (2-PA@MNPs) Functionalization of QxCav-PA@MNPs with PEG

1-PA@MNPs (0.1 g), were dispersed in DMSO (20 ml) and PEG-NHS (50 mg) were added. The suspension was left under stirring condition overnight at 25 °C. The obtained particles were separated magnetically, washed with DMSO, H_2O, ethanol and dried under air.

3.2.6 (3-PA@MNPs) 4PO anchoring on PA_2@MNPs

PA_2@MNPs (0.2 g) and 4PO (5 mg) were dispersed in DMF (10 mL), then $CuSO_4$ (7.5 mg) and (+)-sodium L-ascorbate (40 mg) were added in sequence. The mixture was then kept under constant agitation with an orbital shaker at 25 °C for 16 hours.

Afterwards, 4PO-decorated nanoparticles were separated magnetically, washed with DMF, water and ethanol and at last dried overnight at 25°C.

3.2.7 (4-PA@MNPs) Functionalization of 4PO-PA@MNPs with PEG

3-PA@MNPs (0.1 g), were dispersed in DMSO (20 ml) and PEG-NHS (50 mg) were added. The suspension was left under stirring condition overnight at 25 °C. The obtained particles were separated magnetically, washed with DMSO, H_2O, ethanol and dried under air.

3.3 Samples characterization

3.3.1 XRD

The first characterization step was the XRD analysis (Fig.3.2) of iron oxide MNPs synthesized by the co-precipitation method.

As reported in literature,[3] the position and relative intensity of all diffraction peaks matched well with those of the standard PDF card for magnetite (19-0629), maghemite (39-1346) or any intermediate composition between the two phases.

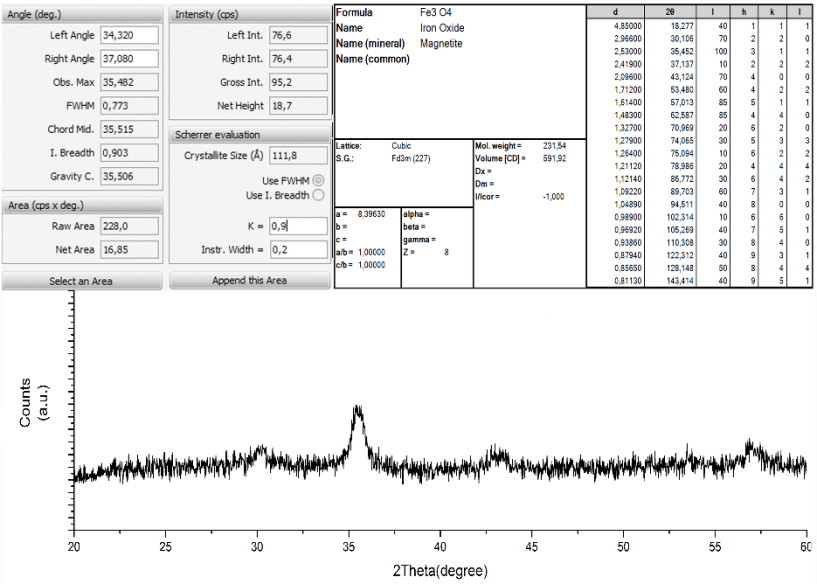

Figure 3. 2: XRD diffraction pattern of bare MNPs with PDF schedule and Debye-Scherrer evaluation of nanoparticles' diameter

Moreover, applying the Debye-Scherrer equation to the main peak it can be possible to evaluate a crystallite size of 15 nm; thus is in line with the average diameter of the particles obtained by TEM measurements.[3]

3.3.2 FT-IR

All the functionalization steps described in the previous paragraph were monitored by FT-IR spectroscopy. Figure

Figure 3.3 and 3.4 compare the nanoparticles covered by a mixed phosphonic monolayers, PA_1@MNPs and PA_2@MNPs, spectra with those of the two decorated systems 2-PA@MNPs and 4-PA@MNPs, respectively.

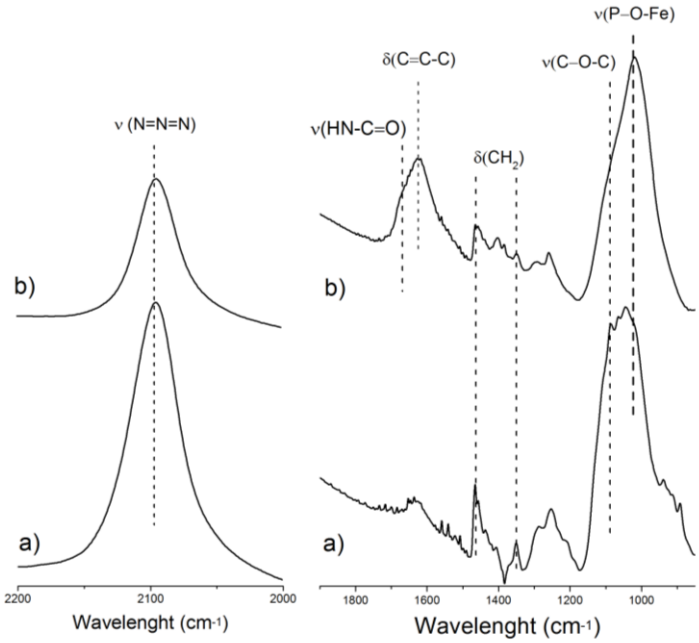

Figure 3. 3: FT-IR comparison between a) PA_1@MNPs, b) 2-PA@MNPs

In all spectra, a single broad and strong band is present at about 1010 cm^{-1} due to P-O-Fe stretching, due to the phosphate bonding group, thus confirming the phosphonic acids bonding to the surface in all samples.

Further information about the functionalization process can be gathered by the peaks in the regions between 2200-2000 and 1900-850 cm^{-1}.

Figure 3.3 shows the comparison between the nanoparticles PA_1@MNPs in which is present with the mixed monolayer of NH_2-PA and N_3-PA (ratio 1:1) and 2-PA@MNPs in which the QxCav was bonded to the mixed monolayer (Figure 3.3 a and b, respectively). Between 2200-2000 cm^{-1} is evident the presence of a strong and narrow peak due to the stretching of N_3 group. Moving from PA_1@MNPs to 2-PA@MNPs there is a decreasing in the intensity of this peak which reflects the decrement of the number of free azido groups due to the "click reaction" that leads to the formation of triazole groups. This behaviour is an indication that the QxCav molecules were anchored onto the surface through the click reaction. Furthermore, in the 1900-850 cm^{-1} region it is possible to detect the presence of a shoulder close to the strong band due to the phosphate group which is characteristic of the C−O−C antisymmetric and symmetric stretches of PEG. Moreover, in the 1700-1600 cm^{-1} range there is a convolution that is due to the bending of C=C-C of aromatic rings, to the stretching of amide group and to the bending of water.

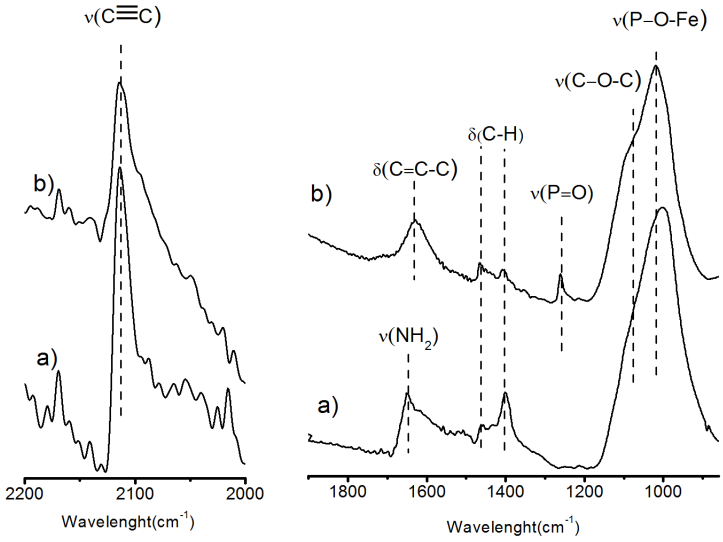

Figure 3. 4: FT-IR comparison between a) PA_2@MNPs, b) 4-PA@MNPs

Figure 3.4, shows the comparison between the PA_2@MNPs nanoparticles having a mixed monolayer of NH_2-PA and HC≡C-PA (ratio 1:1) and 4-PA@MNPs in which the 4-PO cavitand has been bonded to the mixed monolayer (Figure3.4 a and b, respectively). In particular, at about 2100 cm^{-1} it is evident the presence of a strong peak due to the stretching of C≡C group. Similarly to the previous case, moving from PA_2@MNPs to 4-PA@MNPs there is a decreasing of the intensity of this peak that reflects the decrement of the number of free alkyne groups due to the "click reaction", thus

confirming that the 4-PO molecules were anchored onto the surface. In addition, in the spectrum of 4-PA@MNPs a new peak at 1260 cm^{-1} due to P=O stretching of the cavitand is observed, giving a further indication of the cavitand anchoring on the surface.

3.3.3 XPS characterization

The success of the anchoring processes for both the systems is confirmed by XPS characterization. The P2p and N1s spectral regions of PA_1@MNPs and 2-PA@MNPs are shown in Figure 3.5a-b and 3.5c-d whereas Figure 3.6 reports the comparison between PA_2@MNPs and 4-PA@MNPs, Figure 3.6a-b and 3.6c-d respectively. The presence of the P2p band gives information about the phosphonic acid grafting process and its presence at 133.2 eV confirms the formation of a bond between the linker and the surface, in fact this value is typical of phosphonic acids on transition metal oxide surfaces anchored in a bidentate way.[4] As for the 2-PA@MNPs, after QxCav grafting the P2p band is still centred at 133.2 eV, thus indicating that the anchored phosphonic acid is not removed by the click reaction.

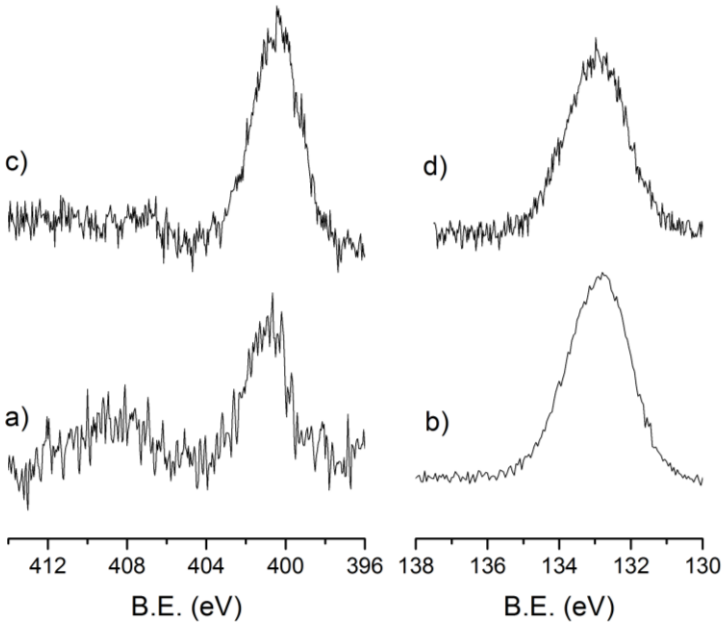

Figure 3. 5: High resolution N1s (left) and P2p (right) XPS spectral regions of a) and b) PA_1@MNPs and c) and d) 2-PA@MNPs

As expected, the PA_1@MNPs in the N1s spectral region (Figure 3.5a) shows a strong signal at 400.8 eV and a second broad and weak peak centred at 408.3 eV that reflects the positively charged N atom of the $–N=N^+=N^-$ azide resonance structure, whilst the envelope around 400.8 eV is due to the convolution of neutral and negatively charged N atoms[5] and to the contribution of the amine terminations. The observed higher B.E. value of the positive N atom in N_3 compared to similar molecules on ZnO could be due to the different

environment such as the different surface and the presence of vicinal amine terminations. Note finally, that the contributions due to the amine groups are likely included in the broad envelope at 400.8 eV and cannot be easily distinguished from the contribution of N_3, even though it seems that the amount of protonated amine terminations is reduced compared to pure amino monolayers.[3] Note that the intensity of the component at about 408.3eV decrease after prolonged XPS irradiation on the contrary, the 2-PA@MNPs (Figure 3.5c) shows single peak at 399.8 eV, shifted towards lower binding energies (B.E.). The observed B.E. value is consistent with the presence of the quinoxalinic ring nitrogen's atoms. Moreover, the signal corresponding to electron deficient N atom of the azido group at 408.3 eV disappeared, indicating that the azide group is consumed in the formation of the triazolic ring, whose signal at about 401eV [5-6] is superimposed with the broad band due to quinoxaline and amidic nitrogens.

Figures 3.6 shows spectra of PA_2@MNPs and 4-PA@MNPs samples. The evolution of P2p region for the two samples is similar to that described for PA_1@MNPs and 2-PA@MNPs, thus confirming the presence of the phosphonic layer. The N1s band of the PA_2@MNPs sample, Figure 3.6a, shows two

components of comparable intensity the one at 399.9 eV due to $–NH_2$ groups of the anchored aminopropylphosphate whilst the component centred at 401.5 eV is due to the amino groups interacting with Fe_3O_4 surface through protonation or formation of -H bonds. The 4-PA@MNPs sample (Figure 3.6c) shows a different pattern due to the presence of N atoms of triazole moiety (~ 401.0 eV) formed after the click reaction and the nitrogen atoms involved in the amidic bond (400.2 eV) between the anchored aminopropylphosphate and the PEG molecules.[47]

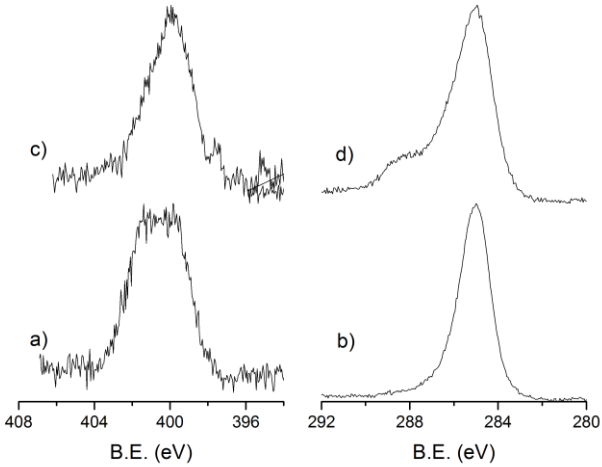

Figure 3. 6: High resolution N1s (left) and P2p (right) XPS spectral regions of a) and b) PA_2@MNPs and c) and d) 4-PA@MNPs

3.4 Removal Test

The removal properties of both samples, 2-PA@MNPs and 4-PA@MNPs, were tested and in the Figure 3.7 is described the pathway used to evaluate their capability to remove two specific pollutants, the 2-aminoanthracene (2AA), as luminescent simulant of aromatic pollutants and the herbicide N,N′-dimethyl-4,4′-bipyridinium dichloride (commercially known as Paraquat). It is possible to split the logical sequence described in Figure 3.7 into two sections, pollutants load (blue line) and nanoparticles renewal with the release (red line) of contaminants compounds. Each of them consist of dispersion through a sonorex of nanoparticles (decorated or not) for 15 minutes, the accumulation with a magnet and the recording of the intensity of the absorbed or emitted radiation from the supernatant liquid (depending on the way a peculiar property of the solution is monitored, with UV-Vis for evaluation of paraquat concentration or Fluorescence spectroscopy for 2-AA).

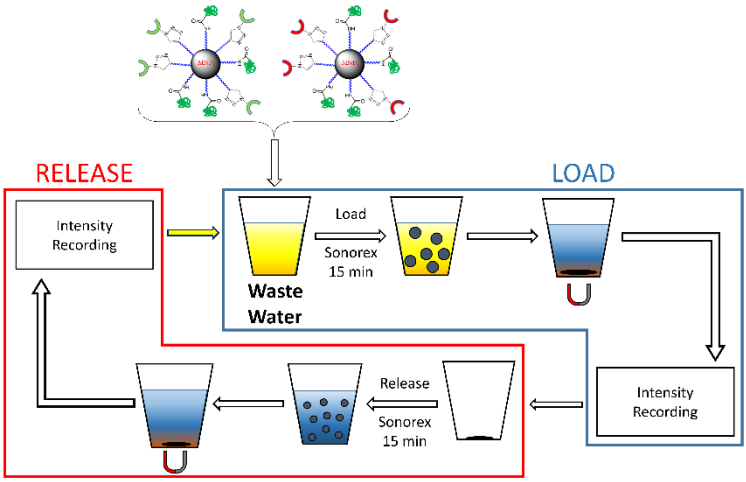

Figure 3. 7: Dispersion pathway used to evaluate removing properties of decorated-nanoparticle

As regard to the removal properties of 2-PA@MNPs, an aqueous solution of 2-AA ($4\times10^{-6}\,M$) was prepared and its emission spectrum was recorded. Figure 3.8 reports the fluorescence of the 2-AA solution after each removing cycle comparing the behaviour of bare nanoparticles (reference sample) and the decorated ones (all data are normalized with the initial intensity of the solution), note that for both samples there is an initial decreasing in the fluorescence intensity of about 80%.

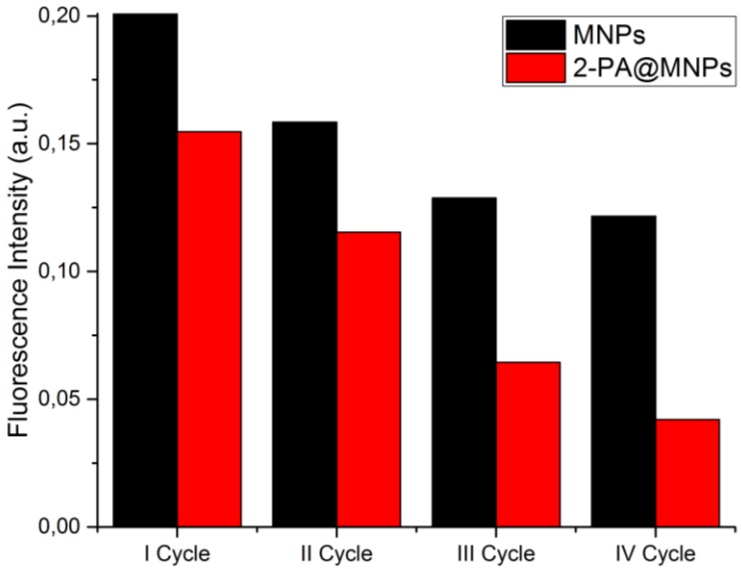

Figure 3. 8: Residual Fluorescence intensity of the 2-AA solution after each load cycle: bare MNPs (black bar) and 2-PA@MNPs (red bar); all data are normalized by the initial intensity of the 2-AA solution.

It can be notice that 2-PA@MNPs have a better removal efficiency. In fact after the fourth cycle MNPs have removed the 87,5% of the initial amount of 2-AA whereas the 2-PA@MNPs the 95%. Thus, is attributable to the complexion properties of the cavitand-based coverage of 2-PA@MNPs.

This different efficiency is confirmed from evaluation of the cumulative amount of released material which correspond to the totally amount of removed pollutants from water (Figure

3.9). From the second cycle on is evident a different behaviour between the two samples due, again, to the different surface coverage. During the first two cycles the released material and, hence, the amount of removed pollutants are similar probably because for high concentration of contaminant the amount of physisorbed molecules on MNPs surface is comparable between the two samples and the presence of QxCav determines only a little increase of the captured material lead. However, after the second cycle the concentration of the contaminant in the solution is strongly reduced and the physisorption process occurring on bare MNPs surface became much less efficient compared the complexation properties occurring in the QxCav cavity of 2-PA@MNPs. Therefore, the amount of removal material continue to increase during third and fourth cycle for 2-PA@MNPs, while it becomes negligible for bare MNPs when pollutant concentration is low.

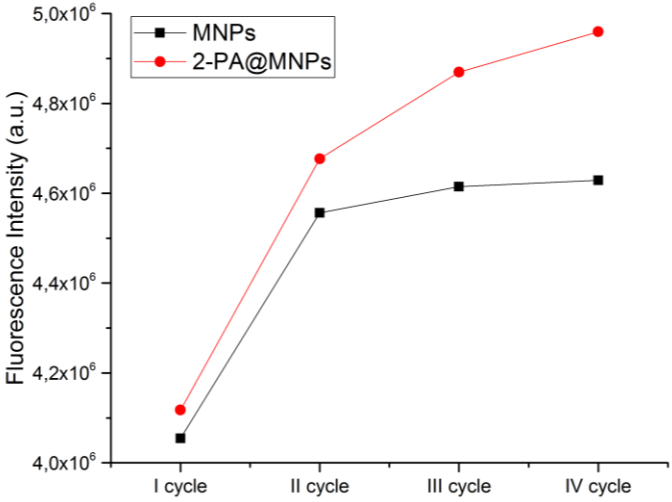

Figure 3. 9: Residual Fluorescence intensity of the 2-AA solution after each release cycle: bare MNPs (black line) and 2-PA@MNPs (red line)

The removal properties of 4-PA@MNPs have been evaluated similarly to 2-PA@MNPS. In this case an aqueous solution of Paraquat ($6\times10^{-5}\,M$) was prepared and its absorption spectrum was recorded. Figure 3.10 reports the absorbance of the water solution contaminated with Paraquat after each removing cycle adopting either the bare MNPs (as reference) or the decorated ones (all data are normalized with the initial intensity of the solution, before the dispersion of the nanoparticles).

This system was monitored for seven cycles because the removal rate of this well-known herbicide from aqueous solution is slower than 2-AA due to its high water solubility (700 g/L at 20 °C). Nonetheless, the 4-PA@MNPs has an excellent removal power if compared with MNPs system. In fact, the bare nanoparticles stop their removing action at about the 52% of the initial concentration of pollutant whereas the 4-PA@MNPs continue cleaning down the solution to the 20%.

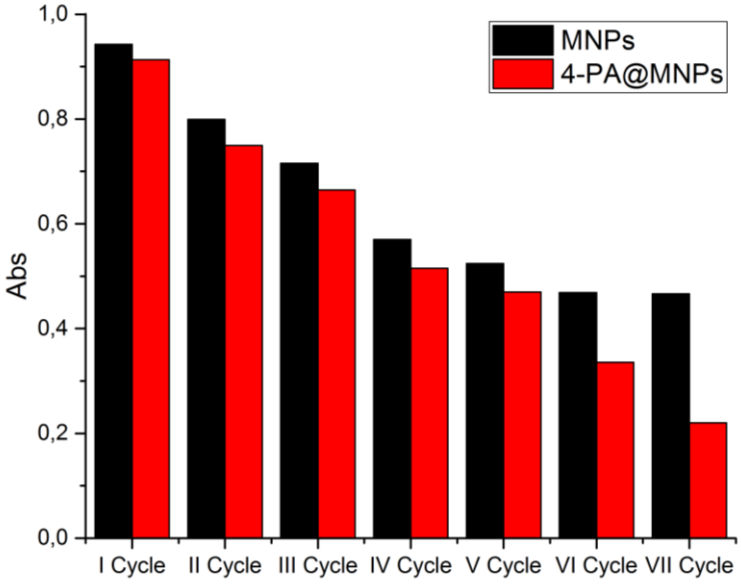

Figure 3. 10: Residual absorbance of Paraquat solution after each load cycle: bare MNPs (black bar) and 4-PA@MNPs (red bar)

Once again, the release, shown in Figure 3.11, is consistent with observed decrease of herbicide concentration in the original solution. Bare MNPs stop releasing Paraquat from fifth cycle, thus indicating that contaminant removal through the physisorption on MNPs surface is no more efficient for low Paraquat concentration, whilst the complexation properties of 4PO cavitand allows an efficient contaminant removal even after VII cycles.

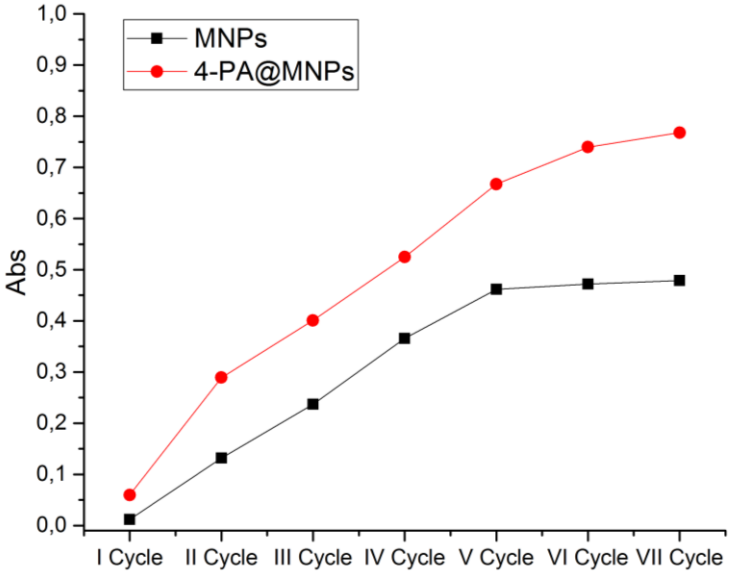

Figure 3. 11: Residual absorbance of Paraquat solution after each release cycle: bare MNPs (black line) and 4-PA@MNPs (red line).

3.5 Conclusions

In this chapter, the synthesis of simple and versatile nanomaterials capable of removing specific pollutants - thanks to the interactions they establish with ad hoc receptor - is reported. The two multifunctional systems have been obtained through a covalent approach. The synthetic pathway consists of two steps: in the first one, the surface of the nanoparticles was covered with a mixed phosphonic monolayer having two different terminal moieties (-C≡CH and -NH_2 or -N_3 and -NH_2, respectively). The mixed phosphonic monolayer is a suitable platform which allow, during the second step, the further anchoring of cavitand molecules (4PO and QxCav), through orthogonal azide–alkyne cycloaddition, and the linkage of PEG molecules, through the amide bond formation. This functionalization improves the stability in aqueous media and the specificity of the decorated-nanoparticles toward either N-methylated or aromatic compounds, respectively. Furthermore, the two systems, 2-PA@MNPS and 4-PA@MNPS were tested to establish their removal power using two target molecules, the 2-Aminoanthracene and the Paraquat, respectively.

Comparing the behaviour of the decorated-nanoparticles with the bare ones, it can be notice that in the case of 2-AA the former decrease the concentration down to the 5% of the initial concentration whilst the latter stop their action at the 12,5%. The tests brought on the Paraquat shown a similar trend, in fact the decorated-nanoparticles lead to a more relevant decrease of the initial concentration if compared with the bare ones.

In conclusion, the pathway used for the synthesis of those material is rapid, reliable and highly versatile, since it allows the fabrication of different systems able to remove various pollutants with a similar approach.

---

[1] Y. S. Kang, S. Risbud, J. F. Rabolt and P. Stroeve, *Chem. Mater., **1996**, 8, 2209-2211.*

[2] M. Dionisio, J. M. Schnorr, V. K. Michaelis, R. G. Griffin, T. M. Swager and E. Dalcanale*, J. Am. Chem. Soc.,* **2012**, 134, 6540-6543.

[3] C. Tudisco, F. Bertani, M. T. Cambria, F. Sinatra, E. Fantechi, C. Innocenti, C. Sangregorio, E. Dalcanale and G. G. Condorelli, *Nanoscale,* **2013**, 5, 11438–11446.

[4] Tudisco, C.; Oliveri, V.; Cantarella, M.; Vecchio, G.; Condorelli, G. G. *Cyclodextrin Anchoring on Magnetic Fe3O4 Nanoparticles Modified with Phosphonic Linkers. Eur. J. Inorg. Chem.* **2012**, 5323–5331.

[5] Gouget-Laemmel, A. C.; Yang, J.; Lodhi M. A.; Siriwardena, A.; Aureau, D.; Boukherroub, R.; Chazalviel, J.-N.; Ozanam, F.; Szunerits S. *Functionalization of Azide-Terminated Silicon Surfaces with Glycans Using Click Chemistry: XPS and FTIR Study. J. Phys. Chem. C* **2013**, 117, 368−375.

[6] *Li, Y.; Wang, J.; Cai, C. Z. Rapid Grafting of Azido-Labeled Oligo(ethylene glycol)s onto an Alkynyl-Terminated Monolayer on Nonoxidized Silicon via Microwave-Assisted "Click" Reaction. Langmuir* ***2011****, 27, 2437−2445.*

Chapter 4: Multifunctional magnetic nanoparticles: a versatile material for enhanced intracellular drug transport

In this chapter, it is reported the synthesis and characterization of multi-functional magnetic nanoparticles (MNPs) usable to enhance intracellular transport of N-methylated drugs.

Fe_3O_4 magnetic core was first functionalized with a monolayer consisting of two different phosphonic acids having acetylene and amino terminal groups, respectively. This layer provides an active platform for further functionalization steps with organic molecules. In particular a tetraphosphonate cavitand receptor (4PO) bearing an azide moiety was anchored on alkyne terminals whereas the N-hydroxysuccinimide activated forms of poly(ethylene glycol) (PEG-NHS), folic acid (FA-NHS) and carboxy-X-rhodamine (Rhod-NHS) were bonded on amine moieties, through 1,3-dipolar cycloaddition and DCC/NHS coupling reactions, respectively.

The obtained MNPs are biocompatible and possess magnetic, luminescent and recognition properties which make them suitable for applications such as multimodal theranostic.

4.1 Introduction

Magnetic nanoparticles are materials of great interest for researchers by virtue of their suitability in a wide range of disciplines, including magnetic fluids,[1] catalysis,[2-3] biotechnology/biomedicine,[4] magnetic resonance imaging,[5-6] data storage,[7] and environmental remediation.[8-9] While a number of methods have been developed for the synthesis of magnetic nanoparticles, successful application of such materials is highly dependent on the stability of the particles under a range of different conditions. In most of the cases, the particles perform best when their size is below a critical value, which is dependent on the material but is typically around 10–20 nm. Such individual nanoparticles have a large constant magnetic moment and behave like a giant paramagnetic atom with a fast response to applied magnetic fields. These features make superparamagnetic nanoparticles very attractive for a broad range of applications, especially biomedical because the

risk of forming agglomerates is negligible at room temperature. However, they show an unavoidable problem that is intrinsic instability over long periods of time. In fact, such small particles tend to form agglomerates to reduce the energy associated with the high surface area to volume ratio. Moreover, naked metallic nanoparticles are chemically highly active, and are easily oxidized in air, resulting generally in loss of magnetism and dispersibility. This suggest that for many applications it is crucial to develop some protection strategies to chemically stabilize the naked magnetic nanoparticles against degradation during or after the synthesis. These strategies comprise grafting or coating with organic species, including surfactants or polymers, or coating with an inorganic layer. It is noteworthy that in many cases the protecting shells not only stabilize the nanoparticles, but can also be used for further functionalization, for instance with other nanoparticles or various ligands, depending on the desired application.

4.2 MNPs for enhanced intracellular drug transport

Nowadays in the field of biomedicine one of the biggest limitation to overcome, in order to exploit thousands of new therapeutics, is the drug-delivery efficiency.

In fact, many pharmaceutical agents such as proteins, enzymes, antibodies and even drugs need to cross the cell membrane in order to exert their therapeutic action. During last decade, lots of strategies have been proposed to deliver those pharmaceuticals inside intracellular milieu but surely the implementation of nanotechnology and in particular nanomaterials to this problem is one of the most promising solution.

In fact, a wide variety of materials having a size range between 1 to 100 nm, including metals, metal oxides, and semiconductors, exhibit unique optical, electrical, and magnetic properties depending on their size and shape. Moreover, the surface of those materials can be easily modified with small molecules, lipids, polymers and other organic

molecules in order to obtain such shuttles capable to cross the barrier.

In this context, iron oxide nanoparticles are very attractive, mainly because the specific magnetic properties of the core and the versatile functionalization of the surface that here are combined in a small-sized object.

4.3 General Procedure

The overall approach for the synthesis of active (6-PA@MNPs) and inactive (5-PA@MNPs) nanosystems is reported in Figure 4.1

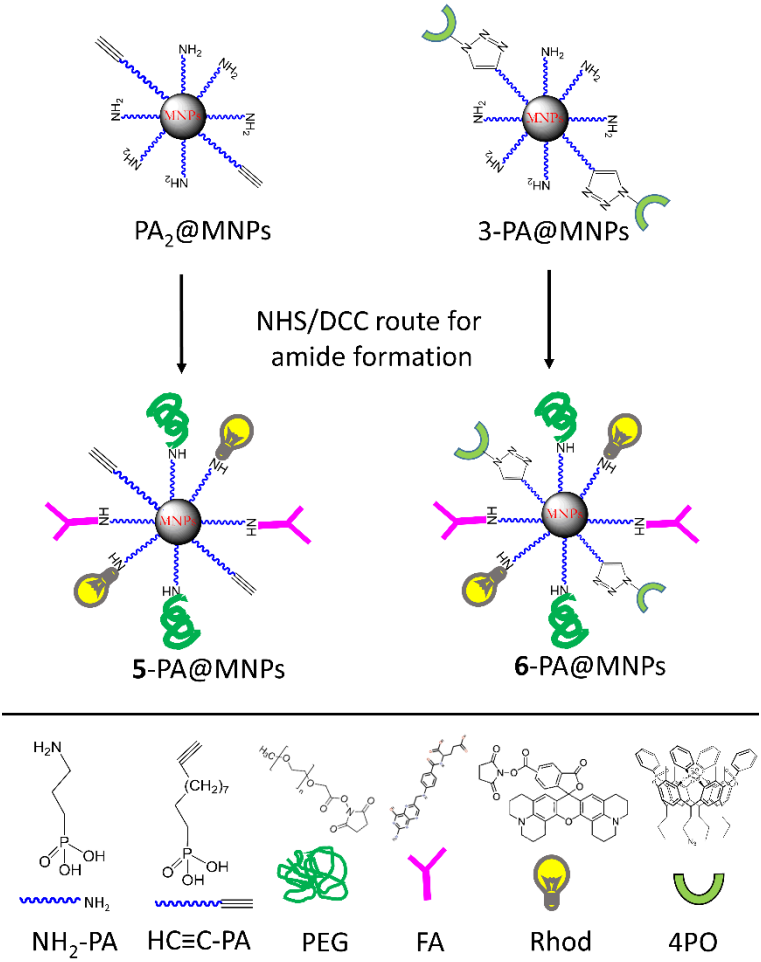

Figure 4. 1: Synthesis of active (6-PA@MNPs) and inactive (5-PA@MNPs) nanosystems

4.3.1 Synthesis of N-Hydroxysuccinimide ester of folic acid (FA-NHS)

FA-NHS was prepared following a published method.[10] FA (500 mg) was dissolved in 10 ml of DMSO with 240 µl of triethylamine. NHS (260 mg) and DCC (470 mg) were added to previous solution and the obtained mixture was kept stirring in dark overnight at room temperature. The by-product, dicyclohexylurea, was removed by filtration. The DMSO solution was then concentrated under reduced pressure and FA-NHS was precipitated in diethyl ether. The product was washed several times with anhydrous ether and dried in air.

4.3.2 MNPs functionalization with PAs mixture

MNPs (200 mg) were dispersed in DMF (25 ml) using an ultrasonic bath for 30 min. 10-undecynylphosphonic acid (C≡C-PA) (100 mg) and 3-aminopropylphosphonic acid (NH_2-PA) (180 mg) were added and the suspension was kept under agitation for 6 h at room temperature. The particles were separated magnetically, washed with DMF, H_2O, ethanol and dried under air.

4.3.3 (5-PA@MNPs) Functionalization of PA@MNPs with FA, Rhod and PEG

PA_2@MNPs (0.1 g), were dispersed in DMSO (20 ml) and FA-NHS (3 mg), Rhod-NHS (1.5 mg) and PEG-NHS (50 mg) were added. The suspension was left under stirring condition overnight at 25 °C. The obtained particles were separated magnetically, washed with DMSO, H_2O, ethanol and dried under air.

4.3.4 (6-PA@MNPs) Functionalization of PA@MNPs with 4PO-N_3, FA, Rhod and PEG

PA_2@MNPs (0.1 g) and 4PO-N_3 (0.02 mmol) were dispersed in DMF (20 mL), then $CuSO_4$ (0.01 mmol) and (+)-sodium L-ascorbate (0.05 mmol) were added in sequence. The mixture was vibrated with an orbital shaker at 25 °C for 24 hours.

Afterwards, 4PO functionalized PA_2@MNPs were separated magnetically washed three times with DMF and once with ethanol and at last dried overnight at 25°C.

Then, 4PO functionalized PA_2@MNPs were functionalized following the same procedure described in the previous paragraph.

4.3.5 (7-PA@MNPs) Functionalization of PA@MNPs with 4PO-N_3, Rhod and PEG

The same procedure described for 6-PA@MNPs but without using folic acid in the last step was used to obtain a cavitand functionalized MNPs analogous.

4.4 Samples characterization

4.4.1 FT-IR

Comparison of FT-IR spectra of PA_2@MNPs, 5-PA@MNPs and 6-PA@MNPs in the 850-1900 cm^{-1} (right) and 2000-2200 cm^{-1} regions (left) are shown in Fig. 4.2. In the FT-IR spectrum of PA_2@MNPs, the presence of a single broad and strong band at ca. 1040 cm^{-1} is due to the phosphate bonding group nonetheless the absence of the P=O stretches (1254 cm^{-1}) and P–O–H stretches (920 cm^{-1}) typical of phosphonic acid powders give confirmation on the actual phosphonic acids bonding to the surface.[11,12,13] In addition, spectra show also two characteristic bands at 1650 cm^{-1} and 2121 cm^{-1}. The first one is associated to the bending vibrations of -NH_2 groups of the amino propyl phosphonic component[14] of the mixed

monolayer whilst the second one is due to the acetylenic group of the alkyne-PA molecule.[11] This observation indicates that the nanosystems preserve both the amino and alkyne terminated groups needed for the subsequent coupling reactions.

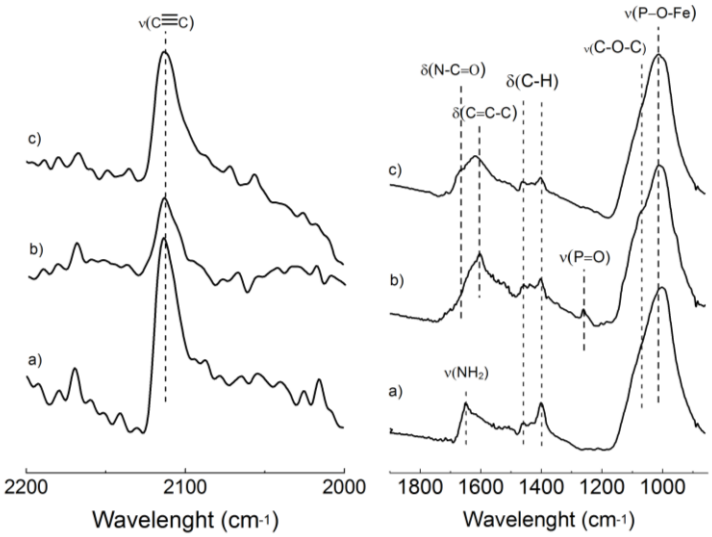

Figure 4. 2: FT-IR spectral regions in the 2000–2200 cm-1 (left) and 850–1900 cm-1 (right) ranges of a) PA_2@MNPs , b) 6-PA@MNPs , c) 5-PA@MNPs.

FT-IR spectrum of 6-PA@MNPs shows a feature at 1250 cm^{-1} due to the presence of free P=O moiety of 4PO,[11] while this

component is absent in the spectrum of 5-PA@MNPs where this receptor is not present. The band convolution around 1630-1600 cm^{-1} is due to the vibrations of amide groups and benzene rings of FA and Rhod.[15,16] The shoulder at 1695 cm^{-1} is assigned to the C=O stretching of the carbonyl groups of FA and Rhod.[17] These peaks indicate the presence of FA and Rhod on both 5-PA@MNPs and 6-PA@MNPs nanosystems. The broad band in the 1150-870 cm^{-1} range is a convolution of the characteristic C−O−C antisymmetric and symmetric stretches of PEG with the strong peak due to the phosphate binding group (ca. 1040 cm^{-1}) of the monolayer. Note that in the case of 6-PA@MNPs a decrease of the characteristic absorption peak of the alkyne group at 2108 cm^{-1} compared to 5-PA@MNPs and PA_2@MNPs is consistent with the occurrence of "click-reaction" between the alkyne moiety and the azide terminations of 4PO.

4.4.2 XPS

The N 1s and C 1s XPS spectral regions of PA_2@MNPs, 5-PA@MNPs and 6-PA@MNPs are shown in Figures 4.3 and 4.4. N 1s band of PA_2@MNPs (Figure 4.3a) consists of two

components of comparable intensity. The component at 399.9 eV is associated to the –NH2 groups of the anchored aminopropylphosphate, whilst the component centered at 401.5 eV, is due to the amino groups interacting with Fe_3O_4 surface through protonation or formation of -H bonds. N 1s band of 6-PA@MNPs (Figure 4.3c) shows a rich structure, due to the presence of nitrogens with different chemical environmental. These new contributions include N atoms of triazole moiety (~ 401.0 eV) formed after the click reaction, the nitrogen atoms involved in the amidic bond (400.2 eV) between the anchored aminopropylphosphate and the FA, PEG and Rhod molecules and N atoms of FA and Rhod (at 399.1 eV and 400.6 eV).[18] The N 1s shape of 5-PA@MNPs (Figure 4.3b) does not change significantly compared to that of 6-PA@MNPs since the contribution of the triazole moiety of 6-PA@MNPs is overlapped with that of the N of the other functional molecules (NH_2-PA, FA, Rhod and PEG).

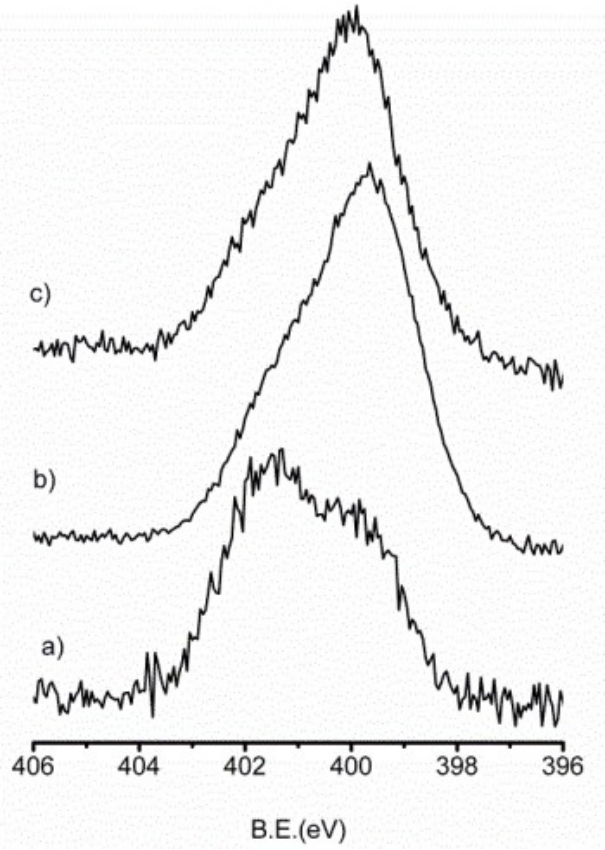

Figure 4. 3: High resolution N 1s XPS spectral regions of (a) PA@MNPs, (b) ***5****-PA@MNPs and (c)* ***6****-PA@MNPs. Intensities were normalized to the Fe* $2p_{3/2}$ *signal.*

The C 1s band (Figure 4.4a) of PA_2@MNPs consists of a single peak at 285.0 eV, assigned to aliphatic carbons. Spectra of 5-PA@MNPs and 6-PA@MNPs (Figure 4.4b,c) show, beside the main peak at 285.0 eV due to aliphatic and aromatic carbons, a shoulder around 286 eV arising from the oxygen-bonded carbons of 4PO and PEG and a component around 288.6 due to carboxylic and amidic groups of FA and Rhod. Note that these last components are more evident on 5-PA@MNPs sample, since in the absence of the large 4PO molecules the steric hindrance on the surface is reduced and an higher amounts of PEG, FA and Rhod molecules can be grafted on the MNPs. The presence of slightly higher amounts of FA and Rhod molecules on 5-PA@MNPs sample is also supported by the higher intensity of the N1s signal compared to the analogous signal of 6-PA@MNPs (Figure 4.3).

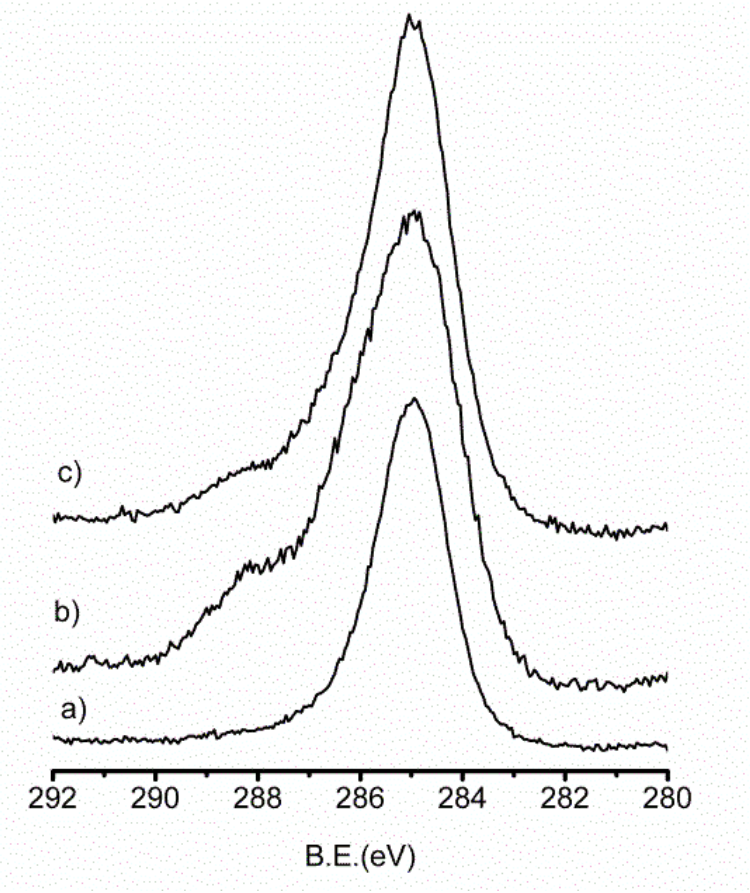

Figure 4. 4: High resolution C 1s XPS spectral regions of (a) PA@MNPs, (b) 5-PA@MNPs and (c) 6-PA@MNPs. Intensities were normalized to the Fe $2p_{3/2}$ signal.

4.4.3 MNPs' features evaluation

Surface characterization apart the MNPs' features were evaluated by TGA, DLS and MTT essay.

The thermogravimetric measurement gives information about the total amount of organic coating. In fact, it is possible to determine the percentage of inorganic and organic content simply increasing the temperature and observing the variation of sample mass. Thermogravimetric curve in the 100-600°C range (Figure 4.5) shows a weight loss of about 8% in the 270-410 °C range.

The mean hydrodynamic size of 6-PA@MNPs was determined by DLS in water and the size distribution (Figure 4.6) consists of a unimodal curve with a polydispersity index of 0.125, a hydrodynamic average size of 60 nm and a zeta potential of -23 mV was also determined. The negative value of the zeta potential is mainly due to the negatively charged core and to the presence of phosphonic acid monolayer.[19,20]

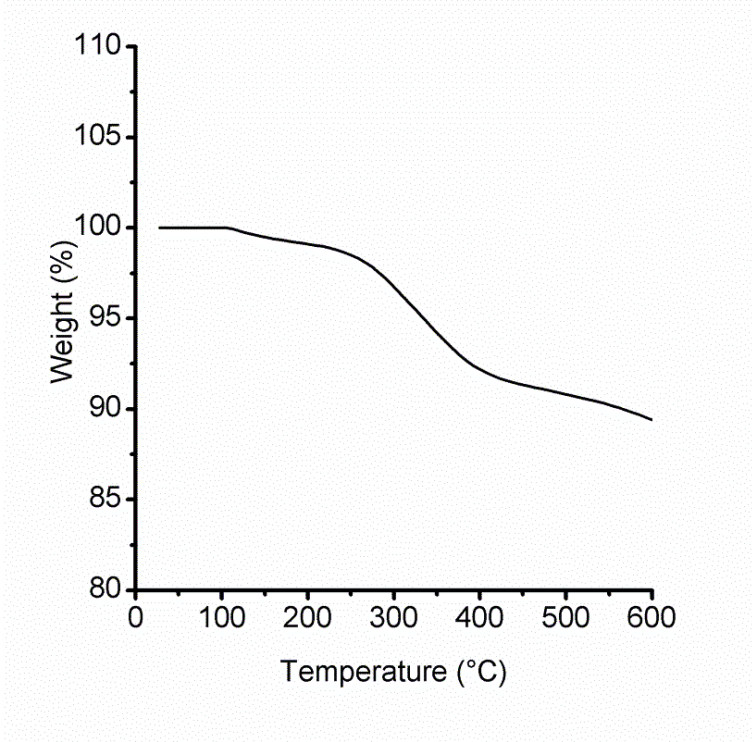

*Figure 4. 5: Thermogram of **6**-PA@MNPs.*

Moreover, cytotoxicity of 5-PA@MNPs and 6-PA@MNPs was evaluated using human mesenchymal stem cells (hMSCs) from adipose tissue. Cell viability was measured using MTT essay after 72h of incubation in the presence of different concentrations of MNPs (20, 40 and 80 μg/ml) (Figure 4.7).

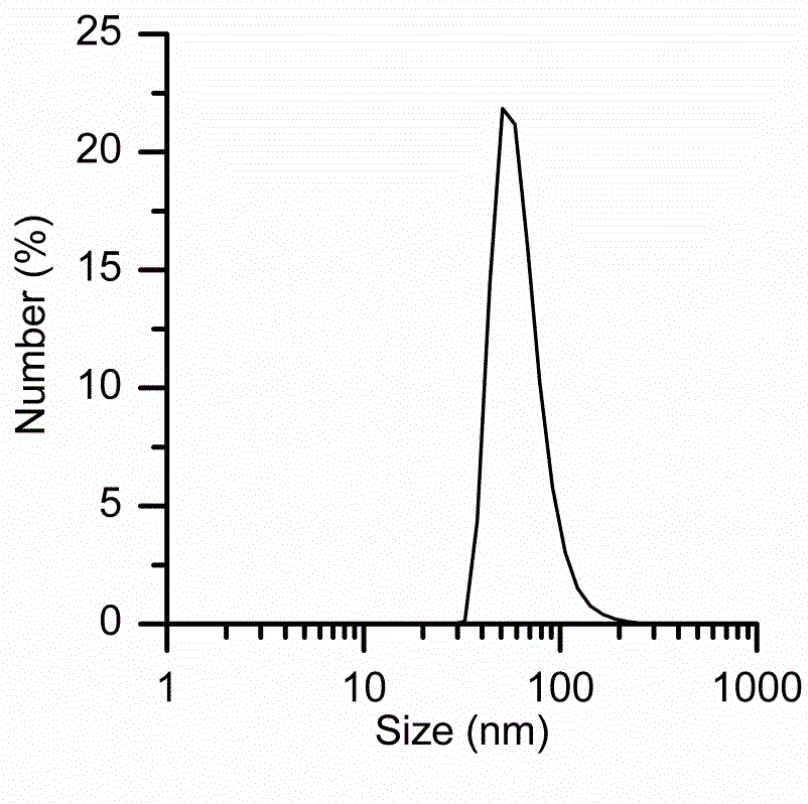

*Figure 4. 6: Size distribution in water of **6**-PA@MNPs.*

The results indicate that hMSCs viability is poorly affected by the presence of MNPs thus indicating that both synthesized systems are biocompatible.

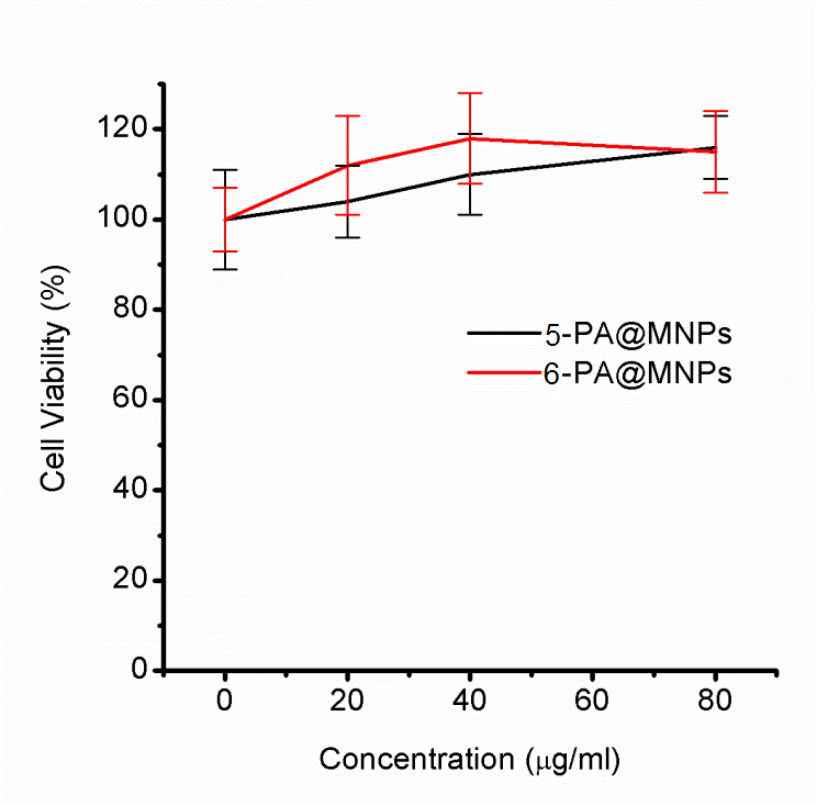

Figure 4. 7; Cell viability of hMSCs evaluated by MTT after 72h of incubation with ***5****-PA@MNPs and* ***6****-PA@MNPs at different concentrations.*

4.5 Cellular interaction tests

The therapeutic application of this system was evaluated following three steps: intracellular uptake, load and release tests carried out with a sample drug and monitoring cells' viability while the loaded-system is inside the cells.

As regarding to intracellular uptake, 6-PA@MNPs (20 μg/mL) were kept in incubation in LoVo cells and monitored by confocal laser scanning fluorescence microscopy after 1, 6, 48, and 72 h of incubation. The obtained results (Figure 4.8) show that the uptake of functionalized MNPs occurs after 1h of incubation and continues even after 6h when an increased amount of internalized MNPs is present. Moreover, an intense fluorescent signal due to Rhodamine bound to MNPs can be observed into cells, with a prevalent location in the cytoplasm.

As for load/release tests, the complexation properties of 6-PA@MNPs were evaluated adopting as antitumor drug the Procarbazine (PCZ), shown in Figure 4.9. The loading step was performed using the hydrochloride form of PCZ (300 μg/ml) that forms a host-guest inclusion complex with the decorated system. Similarly, was performed the loading experiments using the complexation inactive 5-PA@MNPs as blank reference.

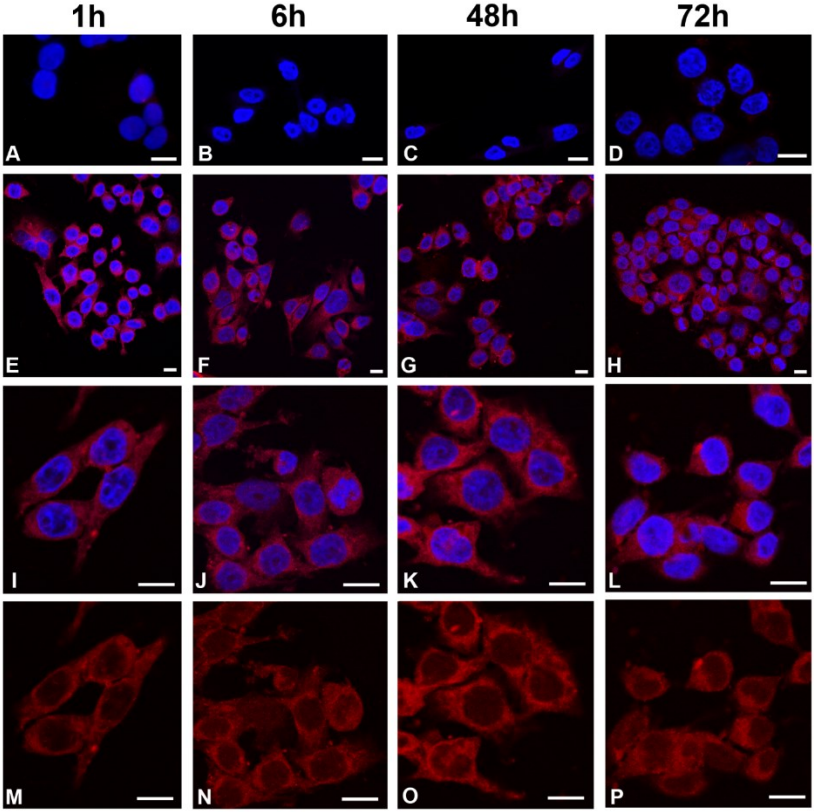

Figure 4. 8: Intracellular uptake of 6-PA@MNPs in LoVo cells. After incubation for 1, 6, 48, and 72h, cells were analysed using a confocal laser scanning microscopy. The signal associated with functionalized MNPs is displayed in red, due to the covalently linked rhodamine. Cell nuclei were stained with DAPI (blue stain). A, B, C, and D: control LoVo cells without nanoparticles. E, F, G, H and their enlargements I, J, K, L: LoVo cells incubated with ***5****-PA@MNPs for the indicated hours. M, N, O, P: the same images in I, J, K, L, respectively, showing only the fluorescence due to the* ***5****-PA@MNPs. Scale bars: 10 µm*

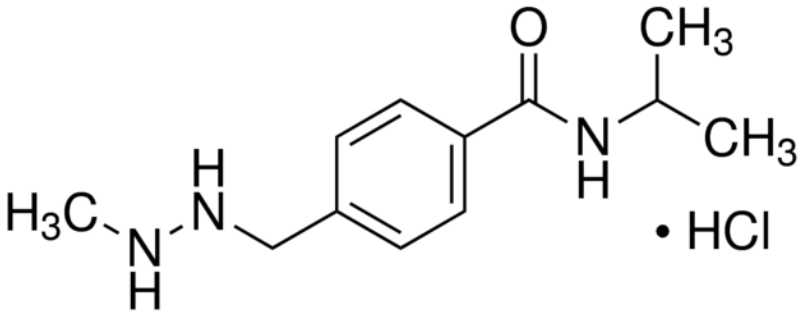

Figure 4. 9: Structure of Procarbazine Hydrochloride

Figure 4.10 compares the release profile (as µg of PCZ per mg of MNPs) of 5-PA@MNPs and 6-PA@MNPs in PBS. The two profiles are significantly different; in fact, 6-PA@MNPs shows an initial rapid release during the first 5 min followed by a continuous release with lower rate in the next 12 h whereas the realising path of 5-PA@MNPs has a lower intensity, very fast and almost complete after 5 minutes. This different behaviour can be explained by considering the amount of the loaded drug as well as the different nature of the drug-coating interactions.

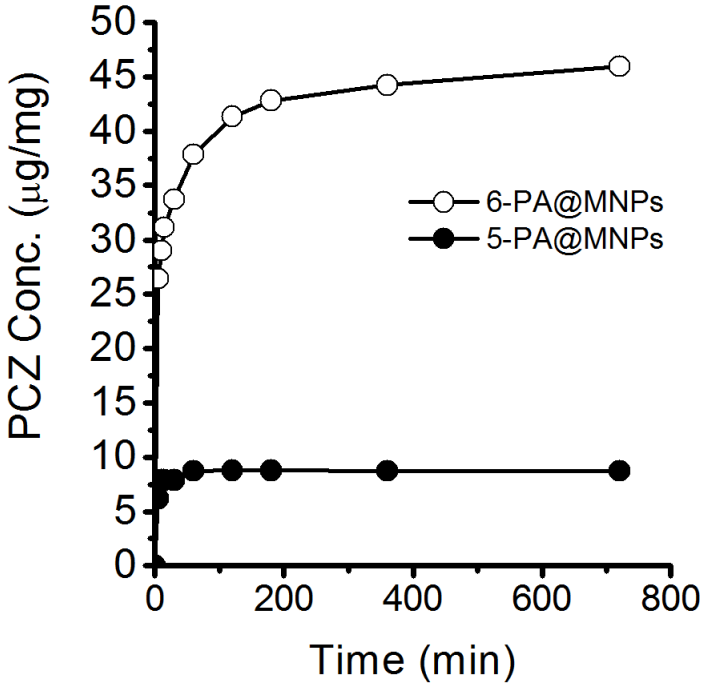

Figure 4. 10: PCZ release profile from ***5****-PA@MNPs and* ***6****-PA@MNPs.*

The amount of PCZ loaded on 5-PA@MNPs, which does not possess suitable receptors, is about 10 μg/mg thus reflects the fact that the loaded drug is only physisorbed on the surface. By contrast, the presence of the cavitand on 6-PA@MNPs surface allows a more efficient loading (about 50 μg/mg, five times higher than 5-PA@MNPs) with a sustained release for longer time, thus indicating that the combination of the

supramolecular interactions between 4PO cavity and N-methylated guest is a key step in determining load-release properties.

Once confirmed the unique properties of cavitand-decorated nanoparticles (in particular recognition and fast cell uptake) specific experiments were thus designed to verify the capability of this system as intracellular vectors for N-methylated drugs (Figure 4.11).

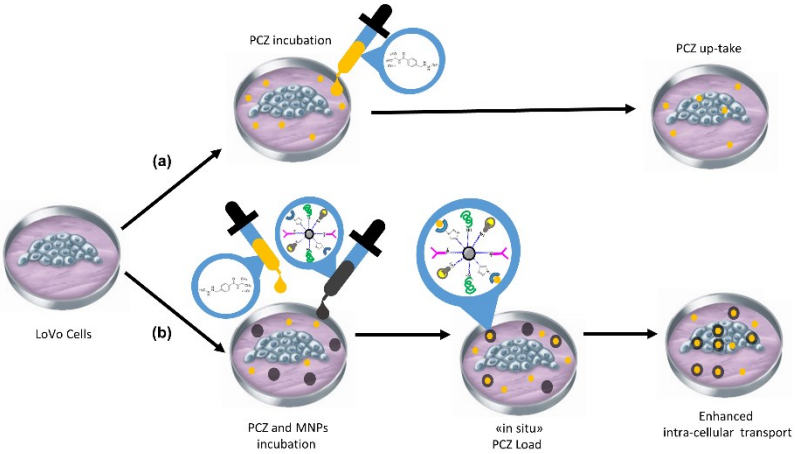

Figure 4. 11: Scheme of the proposed experiment. A PCZ solution and a MNPs suspension were added simultaneously to the LoVo cells. The expected result consists in the load of the drug followed by the internalization of the drug loaded MNPs.

In those experiments, controlled amounts of free PCZ and cavitand-functionalized MNPs were added simultaneously to LoVo cells. The anticancer effect of PCZ was evaluated by

measuring the cell viability at different concentrations of drug and magnetic carriers. In addition, the cytotoxicity of the magnetic carries in the absence of PCZ drug is reported as reference in Figures 4.12a-b.

First of all the experiments in LoVo cells were performed adopting 5-PA@MNPs, which is structurally analogous to cavitand-functionalized MNPs but inactive with respect to drug transport. Plots reported in Figures 4.12c and 4.12e show no difference among the effects obtained by PCZ alone and the drug in combination with 5-PA@MNPs for all the concentrations.

On the other hand, Figures 4.11d and 4.12f compare the cytotoxicity of PCZ at two concentrations (30 and 300 μg/ml) with the cytotoxicity observed by the addition of various concentrations of 6-PA@MNPs (20, 40 and 80 μg/ml). Plots indicate that the simultaneous presence of 6-PA@MNPs and PCZ in the cell culture increase the drug efficacy.

At low PCZ concentrations (30 μg/ml) and 80 μg/ml of 6-PA@MNPs, cell viability is reduced to about 60% after 48h, whilst PCZ's cell viability at the same concentration remains of about 80%. After 72 h cell viability is reduced down to about 50% for all 5-PA@MNPs concentrations, whilst in the absence

of MNPs it is in the 80-90% range (Figure 4.12d). For higher concentration of PCZ (300 μg/ml), the presence of 80 μg/ml of 6-PA@MNPs produces an evident enhancement of PCZ efficiency, reducing cell viability down to 20% after 72h. Lower 6-PA@MNPs concentration (20 μg/ml) does not induce a significant enhancement of PCZ efficiency (Figure 4.12f).

These results confirm that the absence of cavitand receptors precludes an effective PCZ loading on the MNPs surface (see figure 3.10) and, in turn, the MNPs-mediated internalization of the PCZ drug. The different behaviour between cavitand-functionalized 6-PA@MNPs and transport inactive 5-PA@MNPs (summarized in Figure 4.12g-h for the highest concentration) when incubated with N-methylated drugs such as PCZ points out the importance of the combination of the cavitand complexation properties with the internalization capability of MNPs.

Finally, further experiments were performed to evaluate the role of folic acid on MNPs intracellular uptake and on MNPs capability to promote drug internalization. Hereto, a cavitand-functionalized MNPs analogous (7-PA@MNPs) but without folic acid was synthetized following the same path used for 6-PA@MNPs except for the addition of folic acid to the reaction

mixture (see paragraph 4.3 “General Procedure”). The intracellular uptake of 7-PA@MNPs (20 μg mL^{-1}) was monitored after 1, 6, 48, and 72 h of incubation in LoVo cells using confocal laser scanning fluorescence microscopy (Figure 4.13).

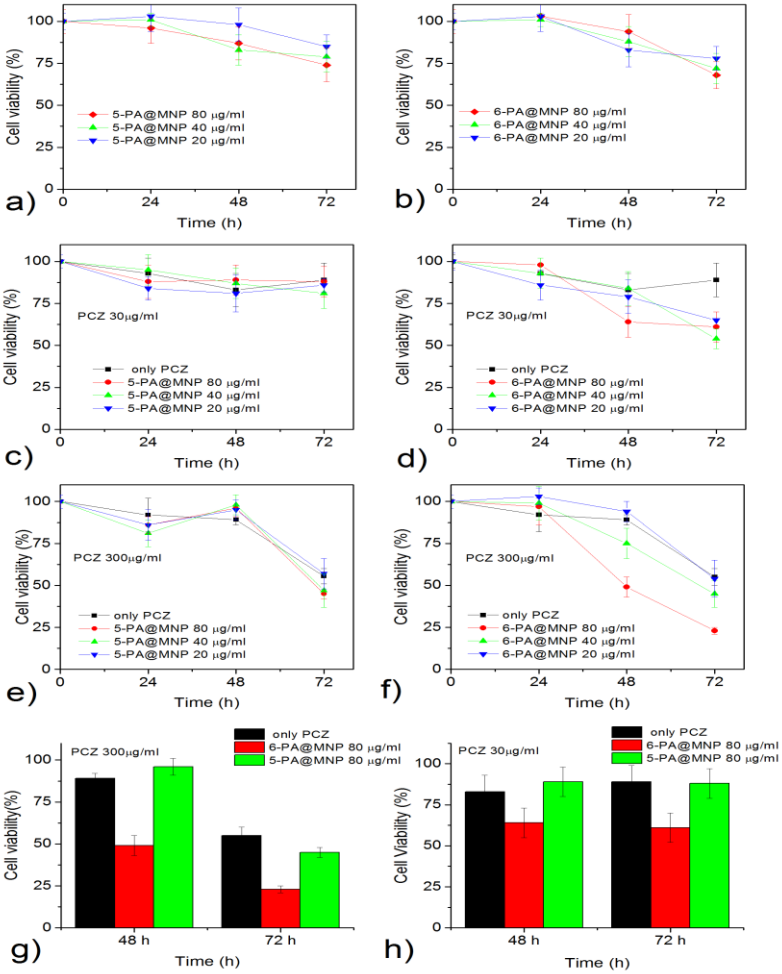

Figure 4. 12: Cell viability (MTT test) of LoVo cells incubated for 24, 48 and 72 h with (a) ***5-****PA@MNPs and (b)* ***6-****PA@MNPs in the absence of antitumor drug; (c-h) with PCZ either alone or in the presence of three concentrations of MNPs (20 μg/ml, 40 μg/ml and 80 μg/ml): (c-d) 30 μg/ml and (e-f) 300 μg/ml PCZ solutions used alone or in the presence of (c and e)* ***5-****PA@MNPs or (d and f)* ***6-****PA@MNPs; Cell viability after 48 and 72h of incubation with g) 30 μg/ml and h) 300 μg/ml PCZ solutions used alone (black bar) or in the presence of 80 μg/ml of 6-PA@MNPs (red bar) or 5-PA@MNPs (green bar).*

The images show a negligible intracellular uptake up to 6 h and a slight MNPs internalization, much less evident if compared to 6-PA@MNPs (Figure 4.10), at 48 and 72 h, thus suggest that folic acid plays a key role on 6-PA@MNPs endocytosis. In order to evaluate the differences between 6-PA@MNPs and 7-PA@MNPs on intracellular drug transport, LoVo cells were exposed to PCZ (300µg/ml) comparing its own behaviour with that of the two samples (Figure 4.14).

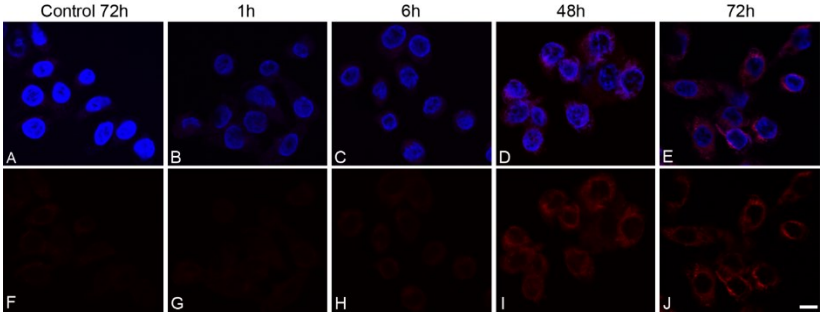

Figure 4. 13: Intracellular uptake of MNPs without folic acid in LoVo cells (7-PA@MNPs). After incubation of 1, 6, 48 and 72h, cells were analyzed using a confocal laser scanning microscope. The signal associated with functionalized MNPs is displayed in red, due to the covalently linked Rhodamine. Cell nuclei were stained with DAPI (blue stain). A: Control LoVo cells after 72h of incubation without nanoparticles. B, C, D, E: LoVo cells incubated with 7-PA@MNPs for 1, 6, 48, 72 hours. F, G, H, I, J: the same images in A, B, C, D, E respectively, showing only the fluorescence due to the eventual presence of 7-PA@MNPs. The scale bar (10 µm) is referred to all images.

Data show that PCZ efficacy is higher if it is combined with 6-PA@MNPs compared to both bare PCZ and PCZ with 7-PA@MNPs. This behaviour is consistent with the observed more efficient intracellular uptake of 6-PA@MNPs with

respect to folic acid-free 7-PA@MNPs, thus confirming the capability of the multifunctional 6-PA@MNPs to act as folic acid assisted intracellular vector for N-methylated drugs.

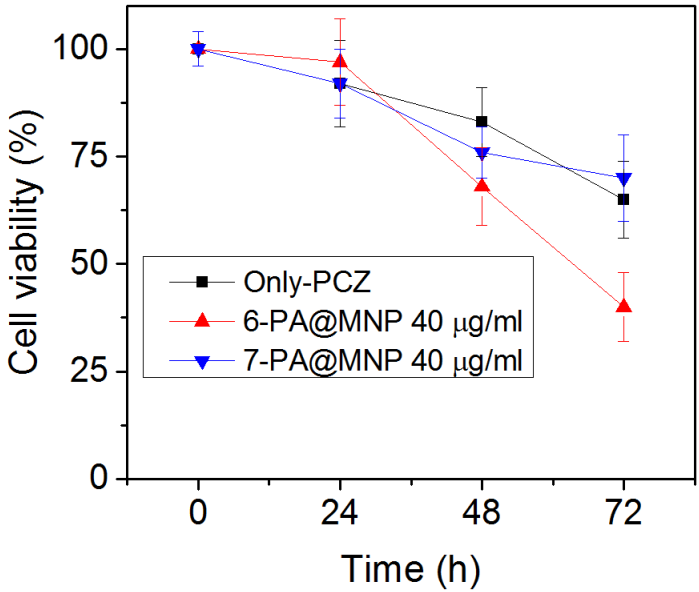

*Figure 4. 14: Cell viability with PCZ (300 μg/ml) used either alone or in the presence of **6-**PA@MNPs or 7-PA@MNPs.*

4.6 Conclusions

In this chapter, we reported the synthesis of new biocompatible MNPs and possessing luminescent and recognition properties, suited for multifunctional theranostic applications. This new system is based on a mixed phosphonic monolayer having two different terminal moieties (-C≡CH, -NH2) which allow the anchoring of various functional molecules (4PO, PEG, FA and Rhod) through orthogonal azide–alkyne cycloaddition and amide bond formation, thus improving the versatility and the multi-functionality of the system. In addition, the rhodamine moieties anchored on the magnetic core makes it a fluorescent probe for optical imaging applications. By exploiting this property, the internalization of functionalized MNPs after incubation in LoVo cells by confocal microscopy was evaluated, showing that internalization is very fast as it already occurs after 1h of incubation. It must be noted that, despite the presence of the hydrophobic 4PO receptor and the rhodamine probe, 6-PA@MNPs proved to be biocompatible, thanks to the presence of the hydrophilic PEG and FA. The potential of this new multi-functional system as enhanced intracellular drug carrier was evidenced by comparing the drug delivery properties of the cavitand-decorated nanoparticles 6-

PA@MNPs with the analogous transport inactive system 5-PA@MNPs. The new synthesized cavitand-decorated 6-PA@MNPs, indeed, are able to recognize and load PCZ, in-situ, acting as a shuttle which promotes the cellular internalization of the drug. These results not only confirm a better loading capability of 6-PA@MNPs compared to 5-PA@MNPs, but also show that the combined use of 6-PA@MNPs with PCZ strongly increases the cytotoxicity of the drug towards malignant cells. Finally, confocal microscopy and cell viability experiments highlight the enhancing effect of the folic acid on intracellular internalization of 6-PA@MNPs. In conclusion, the proposed experiment demonstrates that the difference between success or failure in cancer therapy is often not only due to the used drug, but also how the drug is used.

---

[1] S. Chikazumi, S. Taketomi, M. Ukita, M. Mizukami, H. Miyajima, M. Setogawa, Y. Kurihara*, J. Magn. Magn. Mater.* ***1987****, 65, 245.*

[2] A.-H. Lu, W. Schmidt, N. Matoussevitch, H. BPnnermann, B. Spliethoff, B. Tesche, E. Bill, W. Kiefer, F. SchVth*, Angew. Chem.* ***2004***, *116, 4403; Angew. Chem. Int. Ed.* ***2004****, 43, 4303.*

[3] S. C. Tsang, V. Caps, I. Paraskevas, D. Chadwick, D. Thompsett*, Angew. Chem. 2004, 116, 5763; Angew. Chem. Int. Ed.* ***2004****, 43,* 5645.

[4] A. K. Gupta, M. Gupta*, Biomaterials* ***2005****, 26, 3995.*

[5] S. Mornet, S. Vasseur, F. Grasset, P. Verveka, G. Goglio, A. Demourgues, J. Portier, E. Pollert, E. Duguet*, Prog. Solid State Chem.* ***2006****, 34, 237.*

[6] Z. Li, L. Wei, M. Y. Gao, H. Lei*, Adv. Mater.* ***2005****, 17, 1001.*

[7] T. Hyeon, *Chem. Commun.* ***2003****, 927.*

[8] D. W. Elliott, W.-X. Zhang, *Environ. Sci. Technol.* ***2001****, 35, 4922.*

[9] M. Takafuji, S. Ide, H. Ihara, Z. Xu*, Chem. Mater.* ***2004****, 16, 1977.*

[10] R.J. Lee and P.S. Low*, J. Biological Chem., 1994, 5, 3198-3204.*

[11] C. Tudisco, F. Bertani, M. T. Cambria, F. Sinatra, E. Fantechi, C. Innocenti, C. Sangregorio, E. Dalcanale and G. G. Condorelli, *Nanoscale*, **2013**, 5, 11438–11446.

[12] E. Smecca, A. Motta, M. E. Fragalà, Y. Aleeva and G. G. Condorelli, *J. Phys. Chem. C*, **2013**, 117, 5364-5372

[13] C. Tudisco, V. Oliveri, M. Cantarella, G. Vecchio and G.G. Condorelli, *Eur. J. Inorg. Chem*., **2012**, 32, 5323-5331

[14] S. Manju, C. P. Sharma and K. Sreenivasan, *J. Mater. Chem*., **2011**, 21, 15708-15717.

[15] Y. Zhang, N, Kohler, M. Zhang, *Biomaterials*, **2002**, 23, 1553–1561.

[16] C. Lu, L. R. Bhatt, H. Y. Jun, S. H. Park, K. Y. Chai, *J. Mater. Chem*., **2012**, 22, 19806–19811.

[17] J. Coates, Interpretation of Infrared Spectra, A Practical Approach in *Encyclopedia of Analytical Chemistry, R.A. Meyers Ed., John Wiley & Sons Ltd*, **2000**.

[18] K. Hayashi, K. Ono, H. Suzuki, M. Sawada, M. Moriya, W. Sakamoto and T. Yogo, *ACS Appl. Mater. Interfaces*, **2010**, 2, 1903–1911.

[19] C. Tudisco, F. Bertani, M. T. Cambria, F. Sinatra, E. Fantechi, C. Innocenti, C. Sangregorio, E. Dalcanale and G. G. Condorelli, *Nanoscale*, **2013**, 5, 11438–11446.

[20] S. Mohapatra and P. Pramanik, *Colloids Surf., A*, **2009**, 339, 35–42.

List of Publications:

- C. Tudisco, S. Saccone, M. T. Cambria, E. Fantechi, F. Sinatra, C. Innocenti, F. Bertani, A. Alba, C. Sangregorio, A. E. Giuffrida, E. Dalcanale and G. G. Condorelli, J. Mater. Chem. B, 2015, 3, 4134—4145, DOI: 10.1039/c5tb00547g

- E. Smecca, C. Tudisco, A. E. Giuffrida, M. R. Catalano, A. Speghini, G. Malandrino and G. G. Condorelli Eur. J. Inorg. Chem. 2015, 7, 1261–1268, DOI: 10.1002/ejic.201402479

- Alberti, C. Bongiorno, G. Pellegrino, S. Sanzaro, E. Smecca, G. G. Condorelli, A. E. Giuffrida, G. Cicala, A. Latteri, G. Ognibene, A. Cassano, A. Figoli, C. Spinella and A. La Magna, RSC Adv., 2015,5, 73444-73450 - DOI: 10.1039/C5RA13153G

- C. Tudisco, M. E. Fragalà, A. E. Giuffrida, F. Bertani, R. Pinalli, E. Dalcanale, G. Compagnini, and G. G. Condorelli, J. Phys. Chem. C, 2016, DOI: 10.1021/acs.jpcc.6b03502

Attend Conferences:

1. G. G. Condorelli, M. T. Cambria, A.E. Giuffrida, C. Tudisco, V. Oliveri, S. Saccone, F. Sinatra

   "Design of surface functionalizated Fe3O4 superparamagnetic nanoparticles for intracellular transport"

   XLIV Congresso Nazionale di Chimica Inorganica, Padova, 14 - 17 settembre 2016 ISBN 978 88 6787 624 2

2. M. Torelli, A. Pedrini, F. Bertani, I. Cimatti, L. Poggini, C. Tudisco, A. E. Giuffrida, et al

   "Single Molecule Magnets on Silicon via Self-assembly"

   6th EuChemMS, Seville (Spain), 11-15 September 2016

3. A. E. Giuffrida, C. Tudisco, E. Dalcanale, F. Bertani, G. G. Condorelli

   "Cavitand-decorated superparamagnetic Fe_3O_4 nanoparticles for the removal of aromatic compounds in water"

   6th International Conference on NANO structures and nanomaterials Self-Assembly July 3rd-8th, 2016 - Giardini Naxos (ME), Italy

4. C. Tudisco, M. T. Cambria, A. E. Giuffrida, F. Sinatra, A. Alba, C. D. Anfuso, G. Lupo, A. Falanga, S. Galdiero, C. Satriano, G. G. Condorelli

   "Effects of different surface functionalizations of Fe_3O_4 magnetic nanoparticles for the overcoming of the blood brain barrier"

   E-MRS 2016 Spring Meeting, Congress Center in Lille (France) 2-6 May 2016

5. A. E. Giuffrida, C. Tudisco, G. Compagnini, E. Dalcanale, F. Bertani, A. Di Mauro, M. E. Fragalà, G. G. Condorelli

   "Viable synthetic route towards cavitand-functionalized nanostructured ZnO for molecular recognition"

   4th Nano Today Conference, Dubai, UAE, December 6-10, 2015

6. G. G. Condorelli, C. Tudisco, M. T. Cambria, F. Sinatra, F. Bertani A. Alba, A. E. Giuffrida, S. Saccone, E. Fantechi C. Innocenti, C. Sangregorio, E. Dalcanale

   "Design of magnetic nanoparticles for enhanced intracellular drug transport"

   X INSTM CONFERENCE, Favignana (TP), 28th June – 1st July 2015

7. A. E. Giuffrida, C. Tudisco, E. Dalcanale, F. Bertani, R. Pinalli, A. Di Mauro, M. E. Fragalà, G. G. Condorelli

   "Multistep functionalization of nanocolumnar ZnO films with cavitand receptors through 1,3 dipolar cycloaddition to bifunctional phosphonic linkers"

   E-MRS 2015 Spring Meeting, Congress Center in Lille (France) May 11 - 15, 2015